

Impact of Stochastic Entrainment in the NCAR CAM Deep Convection Parameterization on the Simulation of South Asian Summer Monsoon

RAJU PATHAK (✉ rajuphyamu@gmail.com)

Indian Institute of Technology Delhi <https://orcid.org/0000-0002-2734-4300>

Sandeep Sahany

Indian Institute of Technology Delhi

Saroj Kanta Mishra

Indian Institute of Technology Delhi

Research Article

Keywords: Stochastic Entrainment, South Asian, Parameterization

Posted Date: May 4th, 2021

DOI: <https://doi.org/10.21203/rs.3.rs-473790/v1>

License:   This work is licensed under a Creative Commons Attribution 4.0 International License.

[Read Full License](#)

1 Impact of Stochastic Entrainment in the NCAR CAM Deep Convection Parameterization on the
2 Simulation of South Asian Summer Monsoon

3
4

5
6

Raju Pathak¹, Sandeep Sahany^{1,2}, Saroj Kanta Mishra¹

7
8

Authors Detail

¹Centre for Atmospheric Sciences, Indian Institute of Technology Delhi, India

9
10

²Centre for Climate Research Singapore

11
12

13
14

Corresponding Author

15
16

Raju Pathak

17
18

Centre for Atmospheric Sciences

Indian Institute of Technology Delhi

Hauz Khas, New Delhi, India

19
20

Email: rajuphyamu@gmail.com

21
22
23
24
25
26
27
28
29
30
31
32
33
34
35
36
37
38
39

Abstract

Model simulations are highly sensitive to the formulation of the atmospheric mixing process or entrainment in the deep convective parameterizations used in their atmospheric component. In this paper, we have implemented stochastic entrainment in the deep convection scheme of NCAR CAM5 and analyzed the improvements in model simulation, focusing on the South Asian Summer Monsoon (SASM), as compared to the deterministic entrainment formulation in the default version of the model. Simulations using stochastic entrainment (StochCAM5) outperformed default model simulations (DefCAM5), as inferred from multiple metrics associated with the SASM. StochCAM5 significantly alleviated some of the longstanding SASM biases seen in DefCAM5, such as precipitation pattern and magnitude over the Arabian Sea and western Equatorial Indian ocean, early monsoon withdrawal, and the overestimation (underestimation) in the frequency of light (large-to-extreme) precipitation. Related SASM dynamical and thermodynamical features, such as Somali Jet, low-level westerly winds, and meridional tropospheric temperature gradient (MTTG), are improved in StochCAM5. Further, the simulation of monsoon intra-seasonal oscillation (MISO), Madden Julian Oscillation (MJO), and equatorial Kelvin waves are improved in StochCAM5. Many essential climate variables, such as shortwave and longwave cloud forcing, cloud cover, relative and specific humidity, and precipitable water, show significant improvement in StochCAM5.

40 **1. Introduction**

41 The conventional global climate models (GCMs) have failed to adequately parameterize
42 sub-grid scale cloud and convection processes that occur either in a small region or dissipate
43 instantly (e.g., Jones and Randall 2011). Most current GCMs use a convection parameterization
44 scheme that describes the ensemble mean effects of sub-grid scale convection and cloud processes
45 at the resolved grid-scale while ignoring individual cloud variability (e.g., Palmer 2001; Lin and
46 Neelin 2003; Langan et al. 2014). Previous research has shown that this missing variability is
47 important for realistic simulation of tropical climate systems (e.g., Moncrieff et al. 2012; Waliser
48 et al. 2012) and has used two distinct approaches to incorporate this heterogeneity in GCMs: super-
49 parameterization and stochastic parameterization. For super-parameterization, a cloud-resolving
50 model (CRM) that explicitly resolves sub-grid scale convective processes is used in each GCM
51 grid (e.g., Grabowski and Smolarkiewicz 1999; Khairoutdinov and Randall 2001; Krishnamurthy
52 et al. 2014). On the other hand, for stochastic parameterization, a stochastic term is used in a
53 conventional parameterization scheme (e.g., Buizza et al. 1999; Bright and Mullen 2002; Lin and
54 Neelin 2003; Shutts 2005; Khouider and Majda 2006; Plant and Craig 2008; Khouider et al. 2010;
55 Dorrestijn et al. 2013; Deng et al. 2015). Jones et al. (2019a) developed a different variant of super-
56 parameterization by incorporating multiple CRMs in each GCM grid and initializing each CRM
57 with a unique set of random thermal perturbations (referred to as multiple-instance super-
58 parameterization).

59 Compared to conventional convective parameterization, super-parameterization has made
60 significant advances in weather and climate prediction, especially over the tropics. For example,
61 super parameterization has significantly improved the simulations of Madden Julian Oscillation
62 (MJO; Madden and Julian 1971), tropical precipitation, El-Niño southern oscillation, and tropical

63 cyclones (e.g., Khairoutdinov and Randall 2001; Benedict and Randall 2009, 2011; Stan et al.
64 2010; DeMott et al. 2011, 2013; Pritchard et al. 2011; Arnold et al. 2013; Krishnamurthy et al.
65 2014; Pritchard et al. 2014). Goswami et al. (2015) used super-parameterization in the CFSv2
66 model and reported an improved simulation of intra-seasonal oscillation (ISO) during the South
67 Asian summer monsoon (SASM). However, super-parameterization simulations are
68 computationally expensive, so their use is limited. On the other hand, stochastic parameterization
69 simulations consume computational resources similar to conventional GCMs and outperform
70 them. For example, Goswami et al. (2017a) used the stochastic multi-cloud model scheme (MCM;
71 Khouider et al. 2010; Dorrestijn et al. 2013; Deng et al. 2015) in CFSv2 and reported an improved
72 simulation of tropical synoptic and intra-seasonal variability. Several other researchers also
73 incorporated a stochastic noise term into the grid-scale mean-field and noted an enhanced
74 simulation of tropical diurnal variability and equatorial waves (e.g., Buizza et al. 1999; Bright and
75 Mullen 2002; Lin and Neelin 2003; Shutts 2005; Berner et al. 2009). Wang et al. (2016a, b; 2017)
76 used the stochastic approach of Plant and Craig 2008 in CAM5 to compute the properties of a
77 plume of a given mass stochastically using the Poisson distribution, and they found an improved
78 simulation of precipitation extremes and variability over the tropics.

79 While the above advances in climate modeling, precipitation biases over South Asia,
80 equatorial Indian ocean (EIO), inter-tropical convergence zone (ITCZ), and South Pacific
81 convergence zone (SPCZ) worsen (e.g., Wang et al. 2016a, 2017; Goswami et al. 2017a).
82 Furthermore, simulations of precipitation extremes and inter-annual variability over the Indian
83 subcontinent, quasi-biweekly oscillation (10-20 days), and MISO (30-60 days) need to be
84 improved (e.g., Goswami et al. 2017a,b; Wang et al. 2018). Jones et al. (2019b) also found that

85 using the multiple-instance super-parameterization in GCMs did not improve the simulation of
86 MJO and equatorial waves.

87 Previous research has shown that an adequate representation of the interaction of sub-grid
88 scale cloud and convection processes with large-scale circulations can improve the ISO simulation
89 (e.g., Jiang et al. 2011; DeMott et al. 2011; Abhik et al. 2013). Wang et al. (2018) used the Plant
90 and Craig (2008) scheme in CAM5 to link the stochastic generation of convective clouds to large-
91 scale vertical velocity and reported an improvement in Indian summer monsoon (ISM) simulation
92 but a deterioration in precipitation simulation over the equatorial region. Siebesma et al. (2003)
93 shown that the variation in lateral entrainment rate (i.e., the interaction between the updrafts and
94 the environment) is critical for accounting variability between different updrafts and allowing
95 updrafts to terminate at different levels. It has been found to be sensitive to precipitation extremes,
96 cyclone intensity, climate variability, cloud feedbacks, and climate sensitivity (e.g., Held et al.
97 2007; Knight et al. 2007; Bechtold et al. 2008; Joshi et al. 2010; Yang et al. 2013; Sherwood et al.
98 2014; Qian et al. 2015; Kooperman et al. 2018). For example, Bush et al. (2014) shown that SASM
99 precipitation biases are highly sensitive to entrainment rate using the MetUM model. Oueslati and
100 Bellon (2013) shown that double ITCZ in the Pacific ocean is sensitive to the entrainment rate of
101 convective plumes in the CNRM-CM5 model and that increasing the entrainment rate resulted in
102 a significant reduction in double ITCZ and SPCZ related biases.

103 In general, several attempts have been made to improve entrainment formulations in GCMs
104 (e.g., Neggers et al. 2002; Siebesma et al. 2003; Rio et al. 2010), but most of them do not allow
105 for large variability of entrainment among different updrafts. For example, in Neggers et al. (2002),
106 the entrainment rate is assumed to be the inverse product of updraft vertical velocity and a constant
107 entrainment time-scale. This approach, however, is highly sensitive to the entrainment time-scale

108 specification, and all moist updrafts entrain the environmental air, resulting in a decrease in
109 buoyancy and thereby restricting the updrafts from reaching to neutral buoyancy level (Romps and
110 Kuang 2010). Raymond and Blyth (1986) proposed a different view of entrainment rate
111 formulation that the variability in cloud updrafts can be represented by a stochastic entrainment
112 rate, which has been investigated for shallow convective and non-precipitating convective
113 boundary layer clouds using LES and single-column model (SCM) runs (e.g., Romps and Kuang
114 2010; Nie and Kuang 2012, Sušelj et al. 2013, 2014). Sušelj et al. (2013) used stochastic
115 entrainment in an SCM above the condensation level (LCL) by assuming lateral entrainment as a
116 discrete (rather than a continuous) process and a well-mixed environmental air in the dry updraft
117 region (i.e., below LCL). As a result, the entrainment rate value in the dry updraft region is not
118 sensitive to model results (could be seen in Sušelj et al. 2012) and is set to a constant value for
119 simplicity. This implementation has improved the representation of convective boundary layer
120 clouds in SCM through an improved simulation of turbulent fluxes. In addition to these stochastic
121 entrainment-based LES and SCM runs, the implementation and evaluation of stochastic
122 entrainment rate in a GCM must be thoroughly studied for realistic simulation of global and
123 regional climate.

124 In this study, we implement a stochastic entrainment rate in CAM5's deep convection
125 scheme. In the deep convection scheme, the dilute convective available potential energy (CAPE)
126 is calculated by assuming continuous atmospheric mixing at a constant entrainment rate (Neale et
127 al. 2008). This dilute CAPE is further used in the closure assumption to estimate cloud-base updraft
128 mass-flux and trigger mechanisms (Zhang and McFarlane 1995). As a consequence, implementing
129 a stochastic entrainment rate in CAM5 would also result in stochasticity in closure and trigger
130 mechanism. This study focuses on the impact of stochastic entrainment on SASM simulations as

131 part of an effort to improve SASM and India's climate simulations by the Department of Science
132 and Technology's Centre of Excellence in Climate Modeling at the Indian Institute of Technology
133 Delhi (Dash et al. 2017). The manuscript is organized as follows: Section 1 presents an
134 introduction, Section 2 describes the model details, implementation approach, model simulations
135 and observational data, and Section 3 presents results and discussion. Particularly, in Section 3,
136 we discuss precipitation pattern in Section 3.1, moisture distribution in Section 3.2, cloud
137 properties in Section 3.3, low-level and upper-level wind distribution in Section 3.4, north-south
138 wavenumber frequency spectrum in Section 3.5, and east-west wavenumber frequency spectrum
139 in Section 3.6. Finally, Section 4 concludes the study.

140

141 **2. Model Details, Implementation Approach, Simulations, and Observational Data**

142 **2.1 Model Details**

143 For simulations, the NCAR Community Atmosphere Model version-5.3 (CAM5) is used
144 within the framework of Community Earth System Model version-1.2.2. In CAM5, the finite
145 volume dynamical core, moist turbulence scheme, and shallow convection scheme are used from
146 Lin (2004), Bretherton and Park (2009), and Park and Bretherton (2009, respectively. The revised
147 Zhang-McFarlane (1995) scheme by Neale et al. (2008) to account for the dilute CAPE
148 computation and by Richter and Rasch (2008) to account for the convective momentum transport
149 is used for the treatment of deep convection (hereafter, ZMNR). The stratiform microphysical
150 scheme from Morrison and Gettelman (2008), the ice crystal nucleation from Liu et al. (2007), and
151 the ice supersaturation from Gettelman et al. (2010) are used. The Rapid Radiative Transfer Model
152 (RRTM) is used to calculate the radiative fluxes (Iacono et al. 2008; Mlawer et al. 1997).

153

154 2.2 Implementation Approach

155 In CAM5, the ZMNR scheme is modified to account for the stochastic and discrete nature
156 of the entrainment process, as compared to the prescribed constant entrainment rate across vertical
157 levels. The stochastic entrainment approach used in this paper closely follows the approach used
158 by Sušelj et al. (2013) for convective boundary layer clouds in SCM. We also use Romps and
159 Kuang's (2010) findings that the model results are unaffected by changes in entrainment values
160 below LCL (i.e., in dry updrafts that have a well-mixed environmental air). As a result, the
161 entrainment rate (ε) below LCL is set to a constant value of $0.1 \times 10^{-3} \text{ m}^{-1}$, which is the entrainment
162 rate used in CAM5 (Neale et al. 2008), and the stochastic entrainment rate above the LCL is
163 implemented in the manner described by Sušelj et al. (2013).

164 For a small distance dz ascends of updrafts above LCL, the probability of an entrainment
165 event is determined by a random number (β) drawn from the Bernoulli distribution with a value
166 of zero (representing no entrainment event) or one (representing an entrainment event) with a
167 probability equal to dz/L_0 , where L_0 represents the average distance that the updrafts must
168 traverse to entrain once (or the average distance between two entrainment events). Sušelj et al.
169 (2013) assumed that the fractional entrained mass flux at each entrainment event is proportional
170 to the vertical mass flux of updrafts and equal to $\varepsilon_d M_u$. These assumptions are used to parameterize
171 entrainment rate, as shown in Eq. 1.

$$172 \quad \varepsilon = s\varepsilon_d B\left(\frac{dz}{L_0}\right), \quad (1)$$

173 Further, for a finite distance Δz ascends of updrafts, the number of entrainment events is
174 determined by a random number (φ) drawn from the Poisson distribution with a probability equal
175 to $\Delta z/L_0$, and the profile of entrainment rate is parameterized as shown in Eq. 2.

$$176 \quad \varepsilon(\Delta z) = \frac{1}{\Delta z} \varepsilon_d \varphi \left(\frac{\Delta z}{L_0}\right) \quad (2)$$

177 where, $\frac{1}{\Delta z}$ is the shape parameter since the entrainment profile varies more steeply with height.

178 Based on sensitivity studies for ε_d and L_0 conducted over the SASM and global region, as
179 well as previous studies (Sušelj et al. 2013; Romps and Kuang 2010), the value of L_0 and ε_d are
180 prescribed to $\varepsilon_d = 0.2$ and $L_0 = 100$ m (i.e., each event leads to entrainment of ~20% of the vertical
181 mass flux over an average distance of $L_0 = 100$ m). For simplicity, the distance Δz is considered
182 here as the difference between two vertical model levels. The complete structure of the stochastic
183 entrainment is shown in Figure 1. From the sensitivity studies (see Supp. Figure S1), changing ε_d
184 and L_0 from their original value at the same time has no significant effect on the model results. For
185 example, changing ε_d and L_0 values together from (i) $\varepsilon_d = 0.1$ and $L_0 = 300$ to $\varepsilon_d = 0.2$ and $L_0 =$
186 600 , and (ii) $\varepsilon_d = 0.1$ and $L_0 = 500$ to $\varepsilon_d = 0.2$ and $L_0 = 1000$ results in no significant change in the
187 vertical velocity and humidity over the tropical region. On the other hand, the simulation
188 performed by fixing any one of these parameters (ε_d or L_0) at a time and varying the other
189 parameter shows changes in vertical velocity and humidity distribution. As a result, we anticipate
190 that the model results would be generally sensitive to a single parameter (i.e., either ε_d or L_0)
191 affecting the entrainment rate.

192

193 **2.3 Simulations and Observational Data**

194 We performed two CAM5 simulations, one with the default ZMNR (DefCAM5) and the other
195 with the stochastic ZMNR (StochCAM5). Each simulation is run for 13-years at a horizontal
196 resolution of 0.9° latitude and 1.25° longitude, and 30 vertical levels, with the prescribed
197 climatological monthly sea surface temperature. The first year of simulation is used as a spin-up
198 period, and the remaining 12-years data are used for analysis.

199 The following observations and reanalysis data are used in this study for model evaluation:
200 the Global Precipitation Climatology Project (GPCP; Adler et al. 2003) for monthly total
201 precipitation, the Tropical Rainfall Measuring Mission (TRMM) 3A12 for monthly convective
202 and large-scale precipitation (Kummerow et al. 1998) and 3B42 for daily total precipitation
203 (Huffman et al. 2007). The monthly convective precipitation for GPCP is computed using the total
204 to convective precipitation ratio from TRMM 3A12 (see Pathak et al. 2019 for the methodology
205 used for calculation), and the corresponding large-scale precipitation is obtained by taking out the
206 convective component from total precipitation. In addition, we also use the Clouds and Earth's
207 Radiant Energy System-Energy Balanced and Filled (CERES-EBAF; Loeb et al. 2009) project for
208 shortwave cloud forcing (SWCF) and longwave cloud forcing (LWCF), the National Aeronautics
209 and Space Administration (NASA) Water Vapor Project (NVAP; Randel et al. 1996) for
210 precipitable water and liquid water path, and the high-resolution data series of International
211 Satellite Cloud Climatology Project (ISCCP; Young et al. 2018) for low, middle, high, and total
212 cloud fraction. The horizontal and vertical wind, air temperature, relative humidity, and specific
213 humidity are obtained from the ECMWF reanalysis (ERA-I; Dee et al. 2011). These observed or
214 reanalysis datasets are first linearly interpolated to model resolution, and the climatological mean
215 of these datasets is used for this study.

216

217 **3. Results and Discussion**

218 The DefCAM5 and StochCAM5 simulations are evaluated using the Taylor diagram over
219 the tropics (Figure 2) and Table 1 over the SASM region. Overall, StochCAM5 outperforms
220 DefCAM5 in simulating the oceanic rainfall, shortwave cloud forcing (SWCF), longwave cloud
221 forcing (LWCF), zonal wind at 850 hPa, and vertical wind at 500 hPa over the tropical and SASM

222 region. The frequency distribution of percentage bias for annual mean precipitation (Figure 3)
223 shows that the frequency of large percentage bias (greater than 60%) does not differ much between
224 StochCAM5 and DefCAM5, except for a decrease (increase) in the frequency of moderate
225 percentage bias (30-60%) over tropical land (ocean) in StochCAM5. For the seasonal mean (June-
226 August) precipitation, the frequency of moderate percentage bias (30-60%) and small percentage
227 bias (less than 30%) is greatly reduced over the tropical land but greatly increased the frequency
228 of small percentage bias over the tropical ocean. In general, the large increase in the frequency of
229 small percentage bias over the tropical ocean leads to a significant improvement in precipitation
230 during the SASM period.

231

232 **3.1 Precipitation Pattern**

233 Figure 4 shows the spatial distribution of JJAS mean total, convective, and large-scale
234 precipitation from observations and simulations, as well as their differences. The simulated total
235 precipitation pattern from DefCAM5 and StochCAM5 is found to be comparable to observations,
236 with average values of 4.06, 4.96, and 5.01 mm/day over the tropical region for observations,
237 DefCAM5, and StochCAM5, respectively. The large overestimation over the Arabian Sea (AS),
238 western Indian ocean, and underestimation over the north-east Bay of Bengal (BoB), northeast
239 India, and Indo-Burmese mountains in DefCAM5 are significantly alleviated in StochCAM5, but
240 the overestimation over the leeward side of the Western Ghats (WG) is significantly deteriorated.
241 StochCAM5 also shows a decrease in total precipitation overestimation over SPCZ and ITCZ in
242 the Pacific ocean. These improvements in total precipitation simulation from StochCAM5 are
243 found due to an improved partitioning between convective and large-scale precipitation. For
244 example, StochCAM5 reduces the convective precipitation overestimation and large-scale

245 precipitation underestimation over the majority of South Asia. With StochCAM5, an increase in
246 pattern correlation (PCC) and a decrease in root mean square error (RMSE) are also found for total
247 precipitation (PCC: 0.68; RMSE: 2.96 mm/day), convective precipitation (PCC: 0.74; RMSE: 2.48
248 mm/day) and large-scale precipitation (PCC: 0.42; RMSE: 2.04 mm/day) as compared to
249 DefCAM5 for total precipitation (PCC: 0.63; RMSD: 3.03 mm/day), convective precipitation
250 (PCC: 0.67; RMSE: 2.81 mm/day) and large-scale precipitation (PCC: 0.34; RMSE: 2.16 mm/day)
251 (Figure 4). This is advantageous to the model because the total precipitation biases over South
252 Asia have been a longstanding problem in CAM5 and its predecessors (e.g., Wang et al. 2016a;
253 Anand et al. 2018; Mishra et al. 2018), as well as in CMIP5 (e.g., Sperber et al. 2013). It was not
254 greatly alleviated, even after including stochasticity in the generation of convective clouds (Wang
255 et al. 2016a) and linking it to large-scale vertical velocity (Wang et al. 2018). Further breaking
256 convective precipitation into contributions from the deep and shallow convections (Supp. Figure
257 S2), we find a significant decrease (increase) in deep (shallow) convection over South Asia, except
258 the WG, northeast India, and Indo-Burmese mountains, which show an increase in deep convection
259 in StochCAM5 as compared to DefCAM5. As a result, the improvement in total precipitation
260 simulation over the AS and western Indian ocean from StochCAM5 is due to a decrease in
261 convective precipitation from deep convection, while the worsening over the leeward side of WG
262 is due to an increase in convective precipitation from both deep and shallow convections.

263 In regard to the annual cycle of total precipitation over the Indian land, both DefCAM5
264 and StochCAM5 simulate an earlier monsoon onset (in May), earlier peak precipitation (in mid-
265 June to early-July), and a larger peak precipitation magnitude with respect to observations (Figure
266 5a). However, as compared to DefCAM5, the monsoon withdrawal date (~10 days earlier in
267 DefCAM5) is improved in StochCAM5, but the monsoon onset date (~10 days earlier in

268 DefCAM5) is simulated similar to DefCAM5 with no discernible change (see section 3.4 and
269 Figure 13 for more details), and the peak precipitation magnitude is worsened (approximately 25%
270 greater) in StochCAM5 than DefCAM5 (Figure 5a). The overall deterioration of the annual cycle
271 of total precipitation is largely coming from the Western Ghats due to a large increase in both deep
272 convective precipitation and large-scale precipitation. We speculate that this increase is associated
273 with the corresponding increase in moisture flux convergence (Supp. Figure S3), which is followed
274 by higher deep convection and latent heat release and a positive feedback cycle leading to further
275 convergence and a further increase in total precipitation.

276 Further, the frequency distribution of precipitation rate (Figure 5b) shows that the
277 frequency of light precipitation rate (1-10 mm/day) and moderate precipitation rate (10-20
278 mm/day) in DefCAM5 is overestimated, while the frequency of very heavy (extreme) precipitation
279 rate (greater than 40 mm/day) is underestimated (also seen in CMIP5 models by Jain et al. 2019
280 and Salunke et al. 2019). StochCAM5 improves the frequency distribution of precipitation rate, as
281 well as the contributions of light to extreme precipitation rates to total precipitation (Figure 5c).
282 The improved frequency distribution in StochCAM5 could be to the improved sub-grid scale
283 process representation by launching convective clouds with stochastically varying entrainment
284 rates. The improvement in the frequency distribution of precipitation has also been noted by
285 linking the stochastic Plant and Craig (2008) scheme to large-scale vertical velocity (Wang et al.
286 2018).

287

288 **3.2 Moisture Distribution**

289 Figure 6 shows the JJAS mean vertical cross-section of specific humidity and relative
290 humidity from ERA-I and model simulations, as well as their differences, over 0°-30°N.

291 DefCAM5 shows a positive bias over 40°-70°E and a negative bias over 70°-140°E in the entire
292 troposphere for specific humidity. StochCAM5 alleviates the positive and negative biases seen in
293 DefCAM5 for specific humidity, resulting in a better simulation of specific humidity over the
294 above regions (Figure 6a-c). For relative humidity, StochCAM5 shows a decrease in positive bias
295 over 40°-65°E and a negative bias over 90°-120°E seen in DefCAM5. However, StochCAM5 also
296 shows a deterioration in positive bias over 120°-140°E below 800 hPa for relative humidity (Figure
297 6d-f).

298 Figure 7 shows the JJAS mean total column water vapor (CWV) from NVAP observations
299 and simulations, as well as their differences. DefCAM5 and StochCAM5 both underestimate the
300 CWV over the Indian land, BoB, central and eastern parts of the EIO, and western Pacific ocean,
301 while overestimating the CWV over the Arabian Peninsula, Tibetan region, western AS, and
302 southern Indian ocean. When compared to DefCAM5, StochCAM5 decreases CWV biases over
303 the western AS, southern Indian ocean, and western Pacific ocean while slightly increasing the
304 CWV biases over the Indian land. Overall, the average CWV value over South Asia has been
305 reduced from 42.03 mm in DefCAM5 to 41.99 mm in StochCAM5, resulting in better agreement
306 with 41.84 mm in NVAP observation. In addition, the RMSE of CWV over South Asia has been
307 decreased from 4.9 mm in DefCAM5 to 4.74 mm in StochaCAM5. These CWV improvements
308 are caused by a better distribution of specific humidity from 800 to 200 over western AS and the
309 southern Indian ocean and surface to 600 hPa over BoB and the western Pacific ocean (Figure not
310 shown).

311

312

313

314 3.3 Cloud Properties

315 To understand the factors that influence precipitation and water vapor, we analyze the
316 changes in cloud properties induced by stochastic entrainment. Since the cloud microphysical
317 processes associated with cloud liquid water and ice are used in CAM5 to calculate large-scale
318 precipitation from stratiform clouds (Morrison and Gettelman 2008), in Figure 8, we show the
319 JJAS mean cloud liquid water path (LWP) over South Asia from NVAP observations and
320 simulations, as well as their differences, and in Figure 9, we show the ice water path (IWP)
321 difference between StochCAM5 and DefCAM5. Figure 8 shows that DefCAM5 highly
322 underestimates LWP over northern BoB, eastern EIO, and western Pacific ocean. StochCAM5, on
323 the other hand, alleviates DefCAM5's LWP underestimation over northern BoB, AS, and western
324 Pacific ocean, making it closer to NVAP observations. In addition to the above improvements in
325 LWP, StochCAM5 also shows a deterioration in LWP over the western Indian ocean. Figure 10
326 shows that in StochCAM5, there is a decrease in IWP over the majority of South Asia, with a
327 significant decrease over the western Indian ocean and an increase over WG and northeast India.
328 Overall, the regions of increased LWP and IWP correspond well to regions of increased large-
329 scale precipitation (Figure 4l).

330 Further, we show the difference in detrained liquid water (DLW) and detrained ice water
331 (DICE) over South Asia in Figure 10a, since the DLW and DICE from deep and shallow
332 convection relate to LWP and IWP in large-scale stratiform clouds and convective clouds (e.g.,
333 Morrison and Gettelman 2008; Wang et al. 2016a). We find that StochCAM5 has increased DLW
334 from shallow convection. As this increased DLW is fed into the cloud microphysical
335 parameterization as a source for large-scale cloud ice and water, it increases LWP and IWP
336 (Morrison and Gettelman 2008), and thus the large-scale precipitation. Besides that, StochCAM5

337 has increased the convective mass flux for shallow convection (and thus the increased DLW) and
338 decreased it for deep convection (Figure 10b), resulting in increased shallow convective clouds
339 and decreased deep convective clouds (Figure 10c). These changes in clouds are also reflected in
340 the increased precipitation from shallow convection and the decreased precipitation from deep
341 convection in StochCAM5 (Supp. Figure S2). From Supp. Figure S4, we find that StochCAM5
342 decreases the frequency of occurrence of deep convection while increasing the frequency of
343 occurrence of shallow convection over the tropical and southern subtropical regions. We speculate
344 this could be due to the increased entrainment rate, which results in low buoyancy (as seen from
345 CAPE; Supp. Figure S4) and thus decreased deep convection and moisture in the middle to high
346 levels. Zhang and Mu (2005) also showed that the reduced deep convection favors the build-up of
347 CAPE, which could lead to an increase in the frequency of occurrence of shallow convection.
348 Furthermore, the large decrease in ice clouds in the upper troposphere in StochCAM5 is found to
349 decrease the total cloud ice amount, and possibly it could be one of the reasons for a large decrease
350 in IWP over the majority of South Asia (Figure 10c,d).

351 Figure 11 shows the JJAS mean low, middle, high, and total cloud cover from ISSCP
352 observations and simulations, as well as their differences. In DefCAM5, the low, middle, and high
353 clouds are all overestimated over the Indian land, western and equatorial Indian ocean (Figure 11e-
354 g). However, in StochCAM5 (Figure 11i-k), these overestimations are reduced, particularly in the
355 middle clouds, which are reduced by more than 10% over the western and equatorial Indian ocean,
356 and the high clouds, which are reduced by more than 5% over the Indian land (Figure 11m-o).
357 Thus, the pattern of changes in total clouds is dominated by the changes in middle clouds over the
358 western and equatorial Indian ocean and high clouds over the Indian land (Figure 11p). These
359 changes in the cloud cover in StochCAM5 can also be seen from a relative decrease in relative

360 humidity in middle and high levels (Figure 6f) and the reduced rate of heating and drying the
361 troposphere over 40°-70°E from the moist processes (Supp. Figure S5). This reduced rate of
362 heating and drying the troposphere is arising from the decreased convective updraft mass flux
363 (Figure not shown). Since changes in LWP, IWP, and cloud fraction influences the cloud radiative
364 effects, we find in Supp. Figure S6 that the large negative (positive) bias seen in DefCAM5 over
365 the western Indian ocean and AS in SWCF (LWCF) is significantly alleviated in StochCAM5,
366 with one possible reason being the reduced rate of heating and drying the troposphere (Jones et al.
367 2019b).

368

369 **3.4 Low-level and Upper-level Wind**

370 Since the changes in low-level and upper-level wind circulations during JJAS influence the
371 moisture transport and precipitation over the ISM region, and hence, we analyze the low-level (850
372 hPa) and upper-level (200 hPa) wind circulations from ERA-I and simulations. Both model
373 simulations capture the prime features of low-level wind circulation seen in observation, although
374 with few biases in amplitude and spatial extent (Figure 12a-c). For example, the Somali jet (SJ)
375 and low-level westerly wind over peninsular India and BoB are weaker in DefCAM5, but they are
376 better simulated in StochCAM5 and comparable to ERA-I. In the upper-level wind circulation,
377 DefCAM5 shows a large underestimation in the tropical easterly jet (TEJ) and overestimation in
378 the subtropical westerly jet (STJ). In comparison to DefCAM5, the simulation of STJ is slightly
379 improved, and the simulation of TEJ is deteriorated in StochCAM5 (Figure 12:d-f).

380 To better understand the physical cause of these changes in wind circulation, we show the
381 annual cycle of 600-200 hPa averaged meridional tropospheric temperature gradient (MTTG)
382 between the two boxes, one over 5°N-35°N and 40°E-100°E and other over 5°N-15°S and 40°E-

383 100°E (Figure 13). These two boxes represent the large-scale temperature gradient zones that are
384 responsible for the wind reversal from north-easterly to south-westerly and maintaining the south-
385 westerly wind flow during JJAS (e.g., Webster et al. 1998; Goswami and Xavier 2005; Goswami
386 and Chakravorty 2017). Overall, both model simulates MTTG comparable to ERA-I, but the
387 MTTG reversal from negative to positive and (positive to negative) is ~10 days earlier in
388 DefCAM5 as compared to the observed negative to positive (positive to negative) reversal in ~1st
389 June (~1st October), making the monsoon circulation weaker followed by an early onset and
390 withdrawal of monsoon by ~10 days. The monsoon onset and withdrawal date are defined when
391 MTTG annual cycle changes from negative to positive and positive to negative value, respectively
392 (Goswami and Chakravorty 2017). On the other hand, StochCAM5 simulates the annual cycle of
393 MTTG very similar to ERA-I, except the reversal of negative to positive that is still earlier ~8 days
394 (Figure 13). In StochCAM5, the reversal of MTTG from positive to negative is simulated similarly
395 to ERA-I, resulting in a monsoon withdrawal close to the observed date (~1st October) (e.g., Xavier
396 et al. 2007; Ashfaq et al. 2009). This improvement in MTTG annual cycle in StochCAM5 is
397 thought to be a possible reason for an improvement in SJ and low-level westerly wind. These
398 MTTG changes may be attributed to enhanced regional Hadley circulation (Figure not shown) that
399 improves the meridional and vertical energy transport (Gadgil 2018). Supp. Figure S7 shows the
400 spatial pattern of JJAS mean tropospheric temperature averaged over 700-300 hPa for ERA-I and
401 model simulations. As compared to DefCAM5, StochCAM5 shows a 0.5 K increase in warm bias
402 over the Tibetan region and a 0.25 K increase in cold bias over the southern Indian ocean,
403 indicating an increased north-south temperature gradient and thus a small increase in MTTG peak
404 during JJAS (Figure 13).

405

406 **3.5 North-South Wavenumber-Frequency Spectrum**

407 The pronounced 30-60 day oscillations of northward propagating convection anomalies
408 from EIO to ISM region during JJAS is recognized as a unique feature of monsoon intra-seasonal
409 oscillation (MISO; Joseph et al. 2009; Joseph et al. 2012; Suhas et al. 2012; Abhik et al. 2013;
410 Sharmila et al. 2013; Abhilash et al. 2014). It accounts for ~ 20% of total rainfall variance over the
411 Indo-Pacific region and linked to active and break spells of ISM (e.g., Goswami et al. 2011; Suhas
412 et al. 2013). Hence, the north-south wavenumber frequency spectrum is analyzed during JJAS over
413 the ISM region (65°E-90°E; 15°S-30°N) to investigate how well the DefCAM5 and StochCAM5
414 simulate MISO in comparison to observations. Figure 14a-c shows JJAS north-south space-time
415 spectra of daily precipitation from TRMM and simulations. TRMM shows a dominant northward
416 propagating mode of 30-60 day period at wavenumber 1 with maximum power at 45 days (Figure
417 14a). Compared to TRMM, DefCAM5 failed to capture the MISO signal at wavenumber 1 (Figure
418 14b), while StochCAM5 captures it at wavenumber 1 with maximum power at ~50 days (Figure
419 14c). Further, we compute the ratio of northward and southward power of the precipitation
420 spectrum averaged over 30-90 day period to verify the fraction of meridionally propagating MISO
421 (Figure 14d-f). TRMM shows that the northward power is greater than the southward power at
422 wavenumber 1, while the northward and southward power are nearly equal at all other
423 wavenumbers. DefCAM5 failed to simulate the correct ratio as noticed before, exhibiting higher
424 power for southward not only at wavenumber 1 but also at wavenumber 2. On the other hand,
425 StochCAM5 simulates greater power in northward than southward at wavenumber 1 and 2, but the
426 simulated power is lesser than TRMM.

427 Furthermore, from the analysis of underlying mechanisms for MISO, we find that the
428 MISO improvement in StochCAM5 is likely due to the improvement in the simulation of

429 atmospheric internal dynamics associated with vertical easterly wind shear over the Indian
430 latitudes (Supp. Figure S8; e.g., Jiang et al. 2004; Drbohlav and Wang 2005; Sharmila et al. 2013),
431 and this improvement in MISO could be another reason for the improvements in seasonal mean
432 rainfall (e.g., Abhik et al. 2013; Abhilash et al. 2014).

433

434 **3.6 East-West Wavenumber-Frequency Spectrum**

435 Figure 15 shows the symmetric component of the normalized power spectrum of daily total
436 precipitation averaged over 15°S-15°N during JJAS from TRMM and simulations, using the
437 methodology of Wheeler and Kiladis (1999). This figure shows the eastward and westward
438 propagation of convective anomalies associated with MJO and equatorial waves (e.g., Kelvin and
439 Rossby waves). Previous studies have shown that the zonally (east-west) propagating disturbances
440 travel along the equator and significantly affect the synoptic variability in the tropics. Thus, from
441 figure 15, for MJO, the observed eastward propagating mode with 30-70 days period and wave
442 number 1-5 is found to be weaker simulated (shorter in periodicity and lesser in power, with
443 maximum power only in the zonal wavenumber range of 1-1.5) in DefCAM5, while, it is found to
444 be better simulated with enhancement in power in the zonal wavenumber range of 1-4 in
445 StochCAM5 with an average periodicity of ~30-70 days. This improvement is expected to be
446 arising from increased shallow convection (Zhang and Mu 2005), which helps to precondition the
447 lower troposphere for MJO (e.g., Zhang and Song 2009; Wang et al. 2016b). The power of
448 eastward propagating Kelvin wave is found to be better simulated for lower frequencies (5-25
449 days) at shorter zonal wave-numbers, but the power at higher frequencies for higher zonal wave-
450 numbers is even more underestimated in StochCAM5. Furthermore, for the Rossby wave, a
451 westward propagating wave with periodicity 10-45 days and zonal wavenumber (-1 to -10) is

452 simulated comparable to TRMM, however, the spectral power at smaller zonal wavenumber (-1 to
453 -6) is slightly underestimated in both model simulations.

454

455 **4. Conclusions**

456 In this study, we modified the deterministic ZMNR deep convection parameterization
457 scheme by stochastically formulating the entrainment rate. Two simulations, one with default
458 scheme (DefCAM5) and other with modified scheme (StochCAM5), were performed using
459 NCAR-CAM5. Statistical evaluation metrics computed for these simulations showed that
460 StochCAM5 outperforms DefCAM5 in simulating mean annual and seasonal climate states on
461 both global and regional scales (South Asia). Specifically, StochCAM5 significantly alleviates the
462 South Asian summer monsoon related biases, such as:

- 463 ● The total precipitation overestimation over AS, northeast India, EIO, MC, and the
464 underestimation over central India, BoB, Burmese mountains, Myanmar, and WPO
- 465 ● The early retreat of monsoon from Indian land
- 466 ● The overestimation in the frequency of light to moderate precipitation and underestimation
467 in the frequency of extreme precipitation.

468 These biases have been longstanding concerns in climate modeling, and their improvement will
469 play a crucial role in the simulation of the current climate, process studies, and future climate
470 change projections (e.g., Sperber et al. 2013; Sabeerali et al. 2014; Wang et al. 2018). These
471 improvements in StochCAM5 are due to improved representation of convective clouds by
472 launching clouds with stochastic entrainment rates. In addition to total precipitation, StochCAM5
473 also improves its partitioning between convective and large-scale precipitation components.
474 Improvement in convective precipitation is through the large change in deep- and moderate change

475 in shallow-convective precipitation, while improvement in large-scale precipitation is through
476 improved cloud microphysical properties via LWP (Morrison and Gettelman 2008). Cloud forcing,
477 cloud cover fractions, relative humidity, specific humidity, and precipitable water from
478 StochCAM5 are also considerably improved over South Asia for JJAS.

479 As for the above improvements, StochCAM5 also enhances the large-scale dynamics
480 associated with it. Improved SJ and low-level westerly wind boost the moisture transport from the
481 ocean to the Indian sub-continent (e.g., Findlater 1969), resulting in reduced precipitation biases.
482 The worsening of overestimated precipitation over peninsular India in StochCAM5 as compared
483 to DefCAM5 is due to the strengthening of TEJ and its influence on the low-level westerly jet,
484 thus causing more precipitation over peninsular India and less moisture transport over the core
485 monsoon region (Koteswaram 1958; Sathiyamoorthy 2005; Sreekala et al. 2013). Improvement in
486 large-scale MTTG through the enhancement of meridional and vertical energy transport (Gadgil
487 2018) could be the major reasons for the improvement in low-level wind circulation (e.g.,
488 Goswami and Xavier 2005). This improvement in MTTG enhances the atmospheric instability and
489 convection over the core monsoon region (Zhou and Murtugudde 2014), and hence the
490 improvement in ITCZ (e.g., Gadgil 2018) and monsoon withdrawal (e.g., Xavier et al. 2007;
491 Ashfaq et al. 2009).

492 StochCAM5 has also substantially improved the simulation of MISO, MJO, and planetary-
493 scale equatorial Kelvin waves for higher periodicity days. Thus, we find that although the
494 implementation of stochasticity in cloud entrainment in the deep convection parameterization led
495 to the improvement in multiple climate phenomena, both globally and over South Asia, there still
496 remain biases, suggesting the need for further model development.

497

498 **Acknowledgements**

499 Authors are greatly thankful to the Indian Ministry of Human Resource Development for providing
500 the Ph.D. fellowship to RP. Authors are also thankful to the supercomputing facility
501 (<http://supercomputing.iitd.ac.in/>), DST CoE in Climate Modeling (RP03350), and DST FIST
502 project of CAS at IIT Delhi for providing partial support in the form of computing resources. The
503 NCAR Community Atmosphere Model version-5 (CAM5) used for the model simulations and
504 NCAR-NCL6.4.0 used for data analysis are also acknowledged. Finally, we want to express our
505 gratitude to the five anonymous reviewers for their suggestions, which helped to improve the
506 manuscript.

507

508 **Data Availability**

509 The observed data used in this study is publicly available and the model simulated data can be
510 obtained from the corresponding author.

511

512 **Code Availability**

513 The climate model used for simulations are freely available at <https://www.cesm.ucar.edu/> and the
514 code used for figure generation is available with corresponding author and can be obtained on
515 request.

516

517 **Conflict of interest**

518 The authors declare no competing interests.

519

520

521

522 **References**

- 523 Abhik S, Halder M, Mukhopadhyay P, et al (2013) A possible new mechanism for northward propagation
524 of boreal summer intraseasonal oscillations based on TRMM and MERRA reanalysis. *Clim Dyn*.
525 <https://doi.org/10.1007/s00382-012-1425-x>
- 526 Abhilash S, Sahai AK, Borah N, et al (2014) Prediction and monitoring of monsoon intraseasonal
527 oscillations over Indian monsoon region in an ensemble prediction system using CFSv2. *Clim Dyn*
528 42:2801–2815. <https://doi.org/10.1007/s00382-013-2045-9>
- 529 Adler RF, Huffman GJ, Chang A, et al (2003) The version-2 global precipitation climatology project
530 (GPCP) monthly precipitation analysis (1979-present). *J Hydrometeorol*
531 [https://doi.org/10.1175/1525-7541\(2003\)004<1147:TVGPCP>2.0.CO;2](https://doi.org/10.1175/1525-7541(2003)004<1147:TVGPCP>2.0.CO;2)
- 532 Anand A, Mishra SK, Sahany S, et al (2018) Indian Summer Monsoon Simulations: Usefulness of
533 Increasing Horizontal Resolution, Manual Tuning, and Semi-Automatic Tuning in Reducing
534 Present-Day Model Biases. *Sci Rep* 8:1–14. <https://doi.org/10.1038/s41598-018-21865-1>
- 535 Arnold NP, Kuang Z, and Tziperman E (2013) Enhanced MJO-like variability at high SST. *J. Clim*
536 26:988–1001. doi:10.1175/JCLI-D-12-00272.1.
- 537 Ashfaq M, Shi Y, Tung WW, et al (2009) Suppression of south Asian summer monsoon precipitation in
538 the 21st century. *Geophys Res Lett* 36:1–5. <https://doi.org/10.1029/2008GL036500>
- 539 Bechtold P, Köhler M, Jung T, et al (2008) Advances in simulating atmospheric variability with the
540 ECMWF model: From synoptic to decadal time-scales. *QJRMS*. <https://doi.org/10.1002/qj.289>
- 541 Benedict JJ, Randall DA (2009) Structure of the Madden–Julian Oscillation in the Superparameterized
542 CAM. *J Atmos Sci*. <https://doi.org/10.1175/2009jas3030.1>
- 543 Benedict JJ, Randall DA (2011) Impacts of idealized air–Sea coupling on Madden-Julian oscillation
544 structure in the superparameterized CAM. *J Atmos Sci*. <https://doi.org/10.1175/JAS-D-11-04.1>
- 545 Berner J, Shutts GJ, Leutbecher M, Palmer TN (2009) A spectral stochastic kinetic energy backscatter
546 scheme and its impact on flow-dependent predictability in the ECMWF ensemble prediction system.
547 *J Atmos Sci*. <https://doi.org/10.1175/2008JAS2677.1>
- 548 Boos WR, Kuang Z (2010) Dominant control of the South Asian monsoon by orographic insulation
549 versus plateau heating. *Nature*. <https://doi.org/10.1038/nature08707>
- 550 Bretherton CS, Park S (2009) A new moist turbulence parameterization in the community atmosphere
551 model. *J Clim*. <https://doi.org/10.1175/2008JCLI2556.1>
- 552 Bright DR, Mullen SL (2002) Short-range ensemble forecasts of precipitation during the Southwest
553 monsoon. *Weather Forecast*. [https://doi.org/10.1175/1520-0434\(2002\)017<1080:SREFOP>2.0.CO;2](https://doi.org/10.1175/1520-0434(2002)017<1080:SREFOP>2.0.CO;2)
- 554 Buizza R, Milleer M, Palmer TN (2007) Stochastic representation of model uncertainties in the ECMWF
555 ensemble prediction system. *QJRMS*. <https://doi.org/10.1002/qj.49712556006>
- 556 Bush SJ, Turner AG, Woolnough SJ, et al (2015) The effect of increased convective entrainment on
557 Asian monsoon biases in the MetUM general circulation model. *QJRMS*.
558 <https://doi.org/10.1002/qj.2371>
- 559 Dash, SK. et al (2017) Climate Modeling in India: Present Status and the Way Forward. *BAMS* ES183–
560 ES188. <https://doi.org/10.1175/BAMS-D-16-0322.1>
- 561 Dee DP, Uppala SM, Simmons AJ, et al (2011) The ERA-Interim reanalysis: Configuration and
562 performance of the data assimilation system. *QJRMS* 137:553–597. <https://doi.org/10.1002/qj.828>
- 563 DeMott CA, Stan C, Randall DA (2013) Northward propagation mechanisms of the boreal summer
564

565 intraseasonal oscillation in the ERA-interim and SP-CCSM. *J Clim*. [https://doi.org/10.1175/JCLI-D-](https://doi.org/10.1175/JCLI-D-12-00191.1)
566 [12-00191.1](https://doi.org/10.1175/JCLI-D-12-00191.1)

567 DeMott CA, Stan C, Randall DA, et al (2011) The Asian monsoon in the superparameterized CCSM and
568 its relationship to tropical wave activity. *J Clim*. <https://doi.org/10.1175/2011JCLI4202.1>

569 Deng Q, Khouider B, Majda AJ (2015) The MJO in a coarse-resolution GCM with a stochastic
570 multicloud parameterization. *J Atmos Sci*. <https://doi.org/10.1175/JAS-D-14-0120.1>

571 Dorrestijn J, Crommelin DT, Siebesma AP, Jonker HJJ (2013) Stochastic parameterization of shallow
572 cumulus convection estimated from high-resolution model data. *Theor Comput Fluid Dyn* 27:133–
573 148. <https://doi.org/10.1007/s00162-012-0281-y>

574 Drbohlav HK-L, Wang B (2005) Mechanism of the northward propagating Intraseasonal oscillations:
575 insight from a zonally symmetric model. *J Clim* 18:952–972

576 Findlater J (1969) A major low-level air current near the Indian Ocean during the northern summer.
577 *QJRMS*. <https://doi.org/10.1002/qj.49709540409>

578 Gadgil S (2018) The monsoon system: Land–sea breeze or the ITCZ? *J Earth Syst Sci* 127:1–29.
579 <https://doi.org/10.1007/s12040-017-0916-x>

580 Gettelman A, Liu X, Ghan SJ, et al (2010) Global simulations of ice nucleation and ice supersaturation
581 with an improved cloud scheme in the Community Atmosphere Model. *J Geophys Res Atmos*
582 115:1–19. <https://doi.org/10.1029/2009JD013797>

583 Goswami BB, Khouider B, Phani R, et al (2017a) Improving synoptic and intraseasonal variability in
584 CFSv2 via stochastic representation of organized convection. *Geophys Res Lett*.
585 <https://doi.org/10.1002/2016GL071542>

586 Goswami BB, Khouider B, Phani R, et al (2017b) Improved tropical modes of variability in the NCEP
587 Climate Forecast System (Version 2) via a stochastic multicloud model. *J Atmos Sci*.
588 <https://doi.org/10.1175/JAS-D-17-0113.1>

589 Goswami BB, Krishna RPM, Mukhopadhyay P, et al (2015) Simulation of the Indian Summer Monsoon
590 in the superparameterized Climate Forecast System Version 2: Preliminary results. *J Clim*.
591 <https://doi.org/10.1175/JCLI-D-14-00607.1>

592 Goswami BN, Chakravorty S (2017) Dynamics of the Indian Summer Monsoon Climate. Oxford
593 Research Encyclopedia of Climate Science.
594 <https://doi.org/10.1093/acrefore/9780190228620.013.613>

595 Goswami BN, Wheeler M, Gottschalck JC, Waliser DE (2011) Intra-seasonal variability and forecasting:
596 a review of recent research. *The global monsoon system: research and forecast WMO* 389–4.

597 Goswami BN, Xavier PK (2005) ENSO control on the south Asian monsoon through the length of the
598 rainy season. *Geophys Res Lett* 32:1–4. <https://doi.org/10.1029/2005GL023216>

599 Grabowski WW, Smolarkiewicz PK (1999) CRCP: A Cloud Resolving Convection Parameterization for
600 modeling the tropical convecting atmosphere. *Phys D Nonlinear Phenom*.
601 [https://doi.org/10.1016/S0167-2789\(99\)00104-9](https://doi.org/10.1016/S0167-2789(99)00104-9)

602 Held IM, Zhao M, Wyman B (2007) Dynamic radiative-convective equilibria using GCM column
603 physics. *J Atmos Sci*. <https://doi.org/10.1175/JAS3825.11>

604 Huffman GJ, Adler RF, Bolvin DT, et al (2007) The TRMM Multisatellite Precipitation Analysis
605 (TMPA): Quasi-global, multiyear, combined-sensor precipitation estimates at fine scales. *J*
606 *Hydrometeorol*. <https://doi.org/10.1175/JHM560.1>

607 Iacono MJ, Delamere JS, Mlawer EJ, et al (2008) Radiative forcing by long-lived greenhouse gases:
608 Calculations with the AER radiative transfer models. *J Geophys Res Atmos*.

609 <https://doi.org/10.1029/2008JD009944>
610 Jain S, Salunke P, Mishra SK, Sahany S (2019) Performance of CMIP5 models in the simulation of
611 Indian summer monsoon. *Theor Appl Climatol*. <https://doi.org/10.1007/s00704-018-2674-3>
612 Jiang X, Li T, and Wang B (2004) Structures and mechanisms of the northward propagating boreal
613 summer intraseasonal oscillation. *J Clim* 17:1022–1039. [https://doi.org/10.1175/1520-0442\(2004\)017<1022:SAMOTN>2.0.CO;2](https://doi.org/10.1175/1520-0442(2004)017<1022:SAMOTN>2.0.CO;2).
614
615 Jiang X, Waliser DE, Li JL, Woods C (2011) Vertical cloud structures of the boreal summer intraseasonal
616 variability based on CloudSat observations and ERA-interim reanalysis. *Clim Dyn*.
617 <https://doi.org/10.1007/s00382-010-0853-8>
618 Jones TR, Randall DA (2011) Quantifying the limits of convective parameterizations. *J Geophys Res*
619 *Atmos*. <https://doi.org/10.1029/2010JD014913>
620 Jones, TR, Randall DA, and Branson MD (2019a) Multiple-instance superparameterization. 1: Concept,
621 and predictability of precipitation. *JAMES* 11:3497–3520. <https://doi.org/10.1029/2019ms001610>
622 Jones, TR, Randall DA, and Branson MD (2019b) Multiple-instance superparameterization: 2. The effects
623 of stochastic convection on the simulated climate. *JAMES* 11:3521–3544.
624 <https://doi.org/10.1029/2019MS001611>
625 Joseph S, Sahai AK, Goswami BN (2009) Eastward propagating MJO during boreal summer and Indian
626 monsoon droughts. *Clim Dyn* 32:1139–1153. doi:10.1007/s00382-008-0412-8
627 Joseph S, Sahai AK, Goswami BN, Terray P, Masson S, Luo JJ (2012) Possible role of warm SST bias in
628 the simulation of boreal summer monsoon in SINTEX-F2 coupled model. *Clim Dyn* 38:1561–1576.
629 doi:10.1007/s00382-011-1264-1
630 Joshi MM, Webb MJ, Maycock AC, Collins M (2010) Stratospheric water vapour and high climate
631 sensitivity in a version of the HadSM3 climate model. *Atmos Chem Phys*.
632 <https://doi.org/10.5194/acp-10-7161-2010>
633 Khairoutdinov MF, Randall DA (2001) A cloud resolving model as a cloud parameterization in the
634 NCAR community climate system model: Preliminary results. *Geophys Res Lett*.
635 <https://doi.org/10.1029/2001GL013552>
636 Khouider B, and Majda A J (2006) A simple multcloud parameterization for convectively coupled
637 tropical waves. Part I: Linear analysis. *J Atmos Sci* 63(4):1308–1323.
638 Khouider B, Biello J, Majda AJ (2010) A stochastic multcloud model for tropical convection. *Commun*
639 *Math Sci*. <https://doi.org/10.4310/cms.2010.v8.n1.a10>
640 Knight CG, Knight SHE, Massey N, et al (2007) Association of parameter, software, and hardware
641 variation with large-scale behavior across 57,000 climate models. *Proc Natl Acad Sci USA*.
642 <https://doi.org/10.1073/pnas.0608144104>
643 Kooperman GJ, Pritchard MS, O'Brien TA, and Timmermans BW (2018) Rainfall from resolved rather
644 than parameterized processes better represents the present-day and climate change response of
645 moderate rates in the community atmosphere model. *JAMES* 10:971–988.
646 <https://doi.org/10.1002/2017MS001188>
647 Koteswaram P (1958) The Easterly Jet Stream in the Tropics. *Tellus*.
648 <https://doi.org/10.3402/tellusa.v10i1.9220>
649 Krishnamurthy V, Stan C, Randall DA, et al (2014) Simulation of the South Asian monsoon in a coupled
650 model with an embedded cloud-resolving model. *J Clim*. <https://doi.org/10.1175/JCLI-D-13-00257.1>
651
652 Kummerow C, Barnes W, Kozu T, et al (1998) The Tropical Rainfall Measuring Mission (TRMM) sensor

653 package. *J Atmos Ocean Technol.* <https://doi.org/10.1175/1520->
654 0426(1998)015<0809:TTRMMT>2.0.CO;2

655 Langan R, Archibald R, Plumlee M, et al (2014) Stochastic Parameterization to Represent Variability and
656 Extremes in Climate Modeling. *Procedia Comput Sci.* <https://doi.org/10.1016/j.procs.2014.05.103>

657 Li C, Yanai M (1996) The onset and interannual variability of the asian summer monsoon in relation to
658 land-sea thermal contrast. *J Clim.* 9:358–375

659 Li Y, et al (2018) The Indian Summer Monsoon Intraseasonal Oscillations in CFSv2 Forecasts: Biases
660 and Importance of Improving Air–Sea Interaction Processes. *J Clim* 31(14): 5351-5370.
661 <https://doi.org/10.1175/JCLI-D-17-0623.1>

662 Lin JWB, Neelin JD (2003) Toward stochastic deep convective parameterization in general circulation
663 models. *Geophys Res Lett* 30:1–4. <https://doi.org/10.1029/2002GL016203>

664 Lin SJ (2004) A "vertically Lagrangian" finite-volume dynamical core for global models. *Mon Weather*
665 *Rev.* [https://doi.org/10.1175/1520-0493\(2004\)132<2293:AVLFDC>2.0.CO;2](https://doi.org/10.1175/1520-0493(2004)132<2293:AVLFDC>2.0.CO;2)

666 Liu X et al (2007) (Inclusion of Ice Microphysics in the NCAR Community Atmospheric Model Version
667 3 (CAM3). *J Clim* 20(18):4526-4547. <https://doi.org/10.1175/JCLI4264.1>

668 Loeb NG et al (2009) Toward optimal closure of the earth's top-of-atmosphere radiation budget. *J. Clim.*
669 22(3):748–766.

670 Madden RA, and Julian PR (1971) Detection of a 40–50 day oscillation in the zonal wind in the tropical
671 Pacific. *J Atmos Sci* 28:702–708.

672 Mishra SK, Anand A, Fasullo J, Bhagat S (2018) Importance of the resolution of surface topography in
673 Indian monsoon simulation. *J Clim* 31:4879–4898. <https://doi.org/10.1175/JCLI-D-17-0324.1>

674 Mlawer EJ et al (1997) Radiative transfer for inhomogeneous atmospheres: RRTM, a validated
675 correlated-k model for the longwave. *J Geophys Res* 102(14): 16663-16682.

676 Moncrieff MW, Waliser DE, Miller MJ, et al (2012) Multiscale convective organization and the YOTC
677 virtual global field campaign. *BAMS.* <https://doi.org/10.1175/BAMS-D-11-00233.1>

678 Morrison H, Gettelman A (2008) A new two-moment bulk stratiform cloud microphysics scheme in the
679 community atmosphere model, version 3 (CAM3). Part I: Description and numerical tests. *J Clim.*
680 <https://doi.org/10.1175/2008JCLI2105.1>

681 Neale RB, Richter JH, Jochum M (2008) The impact of convection on ENSO: From a delayed oscillator
682 to a series of events. *J Clim.* <https://doi.org/10.1175/2008JCLI2244.1>

683 Neggers RAJ, Siebesma AP, Jonker HJJ (2002) A multiparcel model for shallow cumulus convection. *J*
684 *Atmos Sci* 59:1655–1668. [https://doi.org/10.1175/1520-0469\(2002\)059<1655:AMMFSC>2.0.CO;2](https://doi.org/10.1175/1520-0469(2002)059<1655:AMMFSC>2.0.CO;2)

685 Nie J, Kuang Z (2012) Responses of shallow cumulus convection to large-scale temperature and moisture
686 perturbations: A comparison of large-eddy simulations and a convective parameterization based on
687 stochastically entraining parcels. *J Atmos Sci.* <https://doi.org/10.1175/JAS-D-11-0279.1>

688 Oueslati B, Bellon G (2013) Convective entrainment and large-scale organization of tropical
689 precipitation: Sensitivity of the CNRM-CM5 hierarchy of models. *J Clim.*
690 <https://doi.org/10.1175/JCLI-D-12-00314.1>

691 Palmer TN (2001) A nonlinear dynamical perspective model error: A proposal for non-local stochastic-
692 dynamic parametrization in weather and climate prediction models. *QJRMS.*
693 <https://doi.org/10.1256/smsqj.57201>

694 Park S, Bretherton CS (2009) The University of Washington shallow convection and moist turbulence
695 schemes and their impact on climate simulations with the community atmosphere model. *J Clim.*
696 <https://doi.org/10.1175/2008JCLI2557.1>

697 Pathak R, Sahany S, Mishra SK, Dash SK (2019) Precipitation Biases in CMIP5 Models over the South
698 Asian Region. *Sci Rep.* <https://doi.org/10.1038/s41598-019-45907-4>

699 Plant RS, Craig GC (2008) A stochastic parameterization for deep convection based on equilibrium
700 statistics. *J Atmos Sci* 65:87–105. <https://doi.org/10.1175/2007JAS2263.1>

701 Pritchard MS, Bretherton CS, and DeMott CA (2014) Restricting 32–128 km horizontal scales hardly
702 affects the MJO in the Superparameterized Community Atmosphere Model v.3.0 but the number of
703 cloud-resolving grid columns constrains vertical mixing. *JAMES* 6:723–739.
704 [doi:10.1002/2014MS000340](https://doi.org/10.1002/2014MS000340)

705 Pritchard MS, Moncrieff MW, Somerville RCJ (2011) Orographic propagating precipitation systems over
706 the united states in a global climate model with embedded explicit convection. *J Atmos Sci.*
707 <https://doi.org/10.1175/2011JAS3699.1>

708 Qian Y, Yan H, Hou Z, et al (2015) Parametric sensitivity analysis of precipitation at global and local
709 scales in the Community Atmosphere Model CAM5. *JAMES.*
710 <https://doi.org/10.1002/2014MS000354>

711 Randel DL, et al (1996) A new global water vapor dataset. *BAMS* 77(6):1233–1246.

712 Raymond DJ, Blyth AM (1986) A stochastic mixing model for non-precipitating cumulus clouds. *J*
713 *Atmos Sci* 43:2708–2718

714 Richter JH and Rasch P (2008) Effects of Convective Momentum Transport on the Atmospheric
715 Circulation in the Community Atmosphere Model, Version 3. *J Clim* 21(7):1487-1499
716 <https://doi.org/10.1175/2007JCLI1789.1>

717 Rio C, Hourdin F, Couvreur F, and Jam A (2010) Resolved versus parametrized boundary-layer plumes.
718 Part II: Continuous formulations of mixing rates for mass-flux schemes. *Bound.-Layer Meteor.*
719 135:469–483.

720 Romps DM, Kuang Z (2010) Do undiluted convective plumes exist in the upper tropical troposphere? *J*
721 *Atmos Sci* 67:468–484. <https://doi.org/10.1175/2009JAS3184.1>

722 Sabeerali CT, Rao SA, George G, et al (2014) Modulation of monsoon intraseasonal oscillations in the
723 recent warming period. *J Geophys Res.* <https://doi.org/10.1002/2013JD021261>

724 Salunke P, Jain S, Mishra SK (2019) Performance of the CMIP5 models in the simulation of the
725 Himalaya-Tibetan Plateau monsoon. *Theor Appl Climatol.* [https://doi.org/10.1007/s00704-018-](https://doi.org/10.1007/s00704-018-2644-9)
726 2644-9

727 Sathiyamoorthy V (2005) Large scale reduction in the size of the Tropical Easterly Jet. *Geophys Res Lett.*
728 <https://doi.org/10.1029/2005GL022956>

729 Sharmila S, Pillai PA, Joseph S, Roxy M, Krishna RPM, Chattopadhyay R, Abhilash S, Sahai AK,
730 Goswami BN (2013) Role of ocean–atmosphere interaction on northward propagation of Indian
731 summer monsoon intra-seasonal oscillations (MISO). *Clim Dyn.* [doi:10.1007/s00382-013-1854-1](https://doi.org/10.1007/s00382-013-1854-1)

732 Sherwood SC, Bony S, Dufresne JL (2014) Spread in model climate sensitivity traced to atmospheric
733 convective mixing. *Nature.* <https://doi.org/10.1038/nature12829>

734 Shutts G (2005) A kinetic energy backscatter algorithm for use in ensemble prediction systems. *QJRM.*
735 <https://doi.org/10.1256/qj.04.106>

736 Siebesma AP, Bretherton CS, Brown A, et al (2003) A large eddy simulation intercomparison study of
737 shallow cumulus convection. *J Atmos Sci.* [https://doi.org/10.1175/1520-](https://doi.org/10.1175/1520-0469(2003)60<1201:ALESIS>2.0.CO;2)
738 0469(2003)60<1201:ALESIS>2.0.CO;2

739 Sperber KR, Annamalai H, Kang IS, et al (2013) The Asian summer monsoon: An intercomparison of
740 CMIP5 vs. CMIP3 simulations of the late 20th century. *Clim Dyn.* <https://doi.org/10.1007/s00382->

741 012-1607-6
742 Sreekala PP, Bhaskara Rao S V., Arunachalam MS, Harikiran C (2014) A study on the decreasing trend
743 in tropical easterly jet stream (TEJ) and its impact on Indian summer monsoon rainfall. *Theor Appl*
744 *Climatol.* <https://doi.org/10.1007/s00704-013-1049-z>
745 Stan C, Khairoutdinov M, Demott CA, et al (2010) An ocean-atmosphere climate simulation with an
746 embedded cloud resolving model. *Geophys Res Lett.* <https://doi.org/10.1029/2009GL040822>
747 Suhas E, Neena JM, Goswami BN (2012) An Indian monsoon intraseasonal oscillations (MISO) index for
748 real time monitoring and forecast verification. *Clim Dyn.* doi:10.1007/s00382-012-1462-5
749 Sušelj K, Hogan TF, Teixeira J (2014) Implementation of a stochastic eddy-diffusivity/mass-flux
750 parameterization into the Navy Global environmental model. *Weather Forecast.*
751 <https://doi.org/10.1175/WAF-D-14-00043.1>
752 Sušelj K, Teixeira J, and Matheou G (2012) EDMF and shallow cumulus boundary layer: An updraft pdf
753 multiple mass flux scheme. *J Atmos Sci* 69:1513–1533.
754 Sušelj K, Teixeira J, Chung D (2013) A unified model for moist convective boundary layers based on a
755 stochastic eddy-diffusivity/mass-flux parameterization. *J Atmos Sci* 70:1929–1953.
756 <https://doi.org/10.1175/JAS-D-12-0106.1>
757 Waliser DE et al (2012) The "year" of tropical convection (May 2008–April 2010): Climate variability
758 and weather highlights. *BAMS* 93:1189–1218. doi:10.1175/2011BAMS3095.1
759 Wang Y, Zhang GJ (2016a) Global climate impacts of stochastic deep convection parameterization in the
760 NCAR CAM5. *JAMES.* <https://doi.org/10.1002/2016MS000756>
761 Wang Y, Zhang GJ, Craig GC (2016b) Stochastic convective parameterization improving the simulation
762 of tropical precipitation variability in the NCAR CAM5. *Geophys Res Lett* 43:6612–6619.
763 <https://doi.org/10.1002/2016GL069818>
764 Wang Y, Zhang GJ, He YJ (2017) Simulation of precipitation extremes using a stochastic convective
765 parameterization in the NCAR CAM5 under different resolutions. *J Geophys Res Atmos*
766 122:12,875-12,891. <https://doi.org/10.1002/2017JD026901>
767 Wang Y, Zhang GJ, Jiang Y (2018) Linking stochasticity of convection to large-scale vertical velocity to
768 improve Indian Summer Monsoon simulation in the NCAR CAM5. *J Clim.*
769 <https://doi.org/10.1175/JCLI-D-17-0785.1>
770 Webster PJ, Magaña VO, Palmer TN, et al (1998) Monsoons: Processes, predictability, and the prospects
771 for prediction. *J Geophys Res Ocean.* <https://doi.org/10.1029/97jc02719>
772 Wheeler M, Kiladis GN (1999) Convectively Coupled Equatorial Waves: Analysis of Clouds and
773 Temperature in the Wavenumber-Frequency Domain. *J Atmos Sci.* [https://doi.org/10.1175/1520-0469\(1999\)056<0374:CCEWAO>2.0.CO;2](https://doi.org/10.1175/1520-0469(1999)056<0374:CCEWAO>2.0.CO;2)
774 Xavier PK, Marzin C, Goswami BN (2007) An objective definition of the Indian summer monsoon
775 season and a new perspective on the ENSO–monsoon relationship. *QJRMS* 133:496.
776 <https://doi.org/10.1002/qj>
777 Yang B, Qian Y, Lin G, et al (2013) Uncertainty quantification and parameter tuning in the cam5 zhang-
778 mcfarlane convection scheme and impact of improved convection on the global circulation and
779 climate. *J Geophys Res Atmos* 118:395–415. <https://doi.org/10.1029/2012JD018213>
780 Young A, et al (2018) The International Satellite Cloud Climatology Project H-Series climate data record
781 product. *Earth Syst Sci Data* 10:583–593. <https://doi.org/10.5194/essd-10-583-2018>, 2018.
782 Zhang GJ, and Mu M (2005) Effects of modifications to the Zhang-McFarlane convection
783 parameterization on the simulation of the tropical precipitation in the National Center for
784

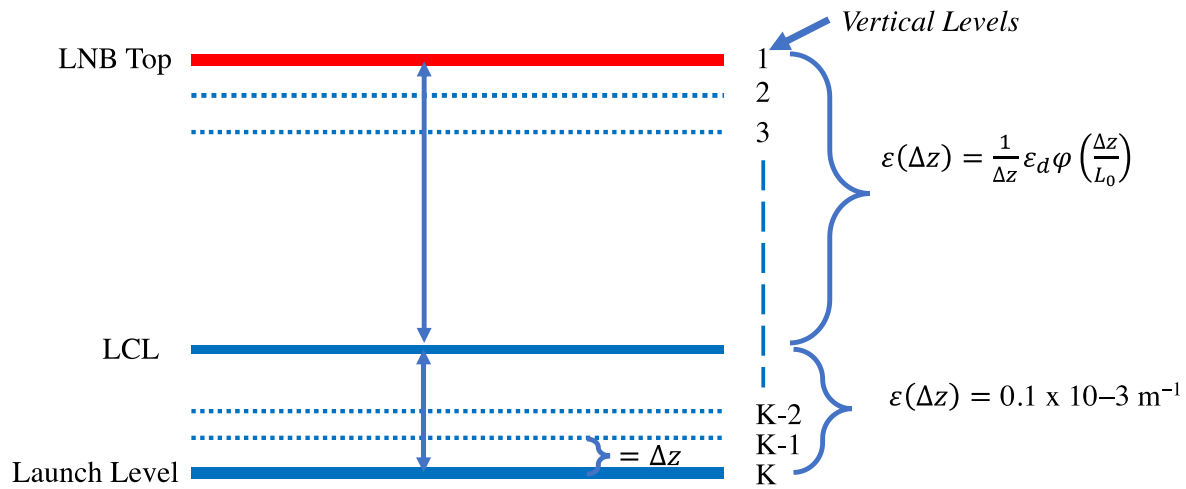
785 Atmospheric Research Community Climate Model, version 3. J Geophys Res 110:D09109.
786 doi:10.1029/2004JD005617.
787 Zhang GJ, and Song X (2009) Interaction of deep and shallow convection is key to Madden-Julian
788 Oscillation simulation. Geophys Res Lett 36:L09708. doi:10.1029/2009GL037340.
789 Zhang GJ, McFarlane NA (1995) Sensitivity of climate simulations to the parameterization of cumulus
790 convection in the canadian climate centre general circulation model. Atmos - Ocean.
791 <https://doi.org/10.1080/07055900.1995.9649539>
792 Zhou L, Murtugudde R (2014) Impact of northward-propagating intraseasonal variability on the onset of
793 Indian summer monsoon. J Clim. <https://doi.org/10.1175/JCLI-D-13-00214.1>
794

795 Table 1: List of statistical values computed over South Asia from observation/ERA-I, DefCAM5
 796 and StochCAM5.
 797

	Obs./ERA-I Mean	DefCAM5 (StochCAM5) Mean	Pearson Pattern Correlation	Normalized Standard Deviation	Percentage Bias	RMSE
Land Rainfall	3.91	4.62 (5.02)	0.68 (0.70)	1.16 (1.33)	17.95 (29.29)	3.37 (3.73)
Ocean Rainfall	4.13	5.15 (5.00)	0.58 (0.70)	0.83 (0.82)	24.79 (21.58)	2.83 (2.43)
SWCF	-50.35	-62.91 (-59.98)	0.81 (0.83)	1.09 (1.08)	24.96 (19.13)	22.67 (20.26)
LWCF	35.59	35.19 (32.61)	0.82 (0.86)	0.89 (0.82)	-1.11 (-8.35)	12.14 (11.03)
Land 2-m Temperature	24.02	24.74 (24.80)	0.94 (0.94)	1.04 (1.07)	2.97 (3.25)	2.73 (2.77)
T (1000-100 hPa)	26.56	24.65 (24.69)	0.46 (0.47)	1.35 (1.38)	-7.21 (-7.05)	5.18 (5.21)
Relative Humidity (1000-100 hPa)	71.78	72.09 (71.92)	0.91 (0.91)	0.99 (1.00)	0.45 (0.20)	7.46 (7.39)
Zonal Wind at U850	4.36	-0.23 (.05)	0.95 (0.96)	1.08 (1.12)	-105.36 (98.83)	4.88 (4.65)
Vertical Wind at 500 hPa	-0.027	-0.017 (-0.02)	0.36 (0.40)	0.70 (0.73)	-35.65 (-37.49)	0.05 (0.05)

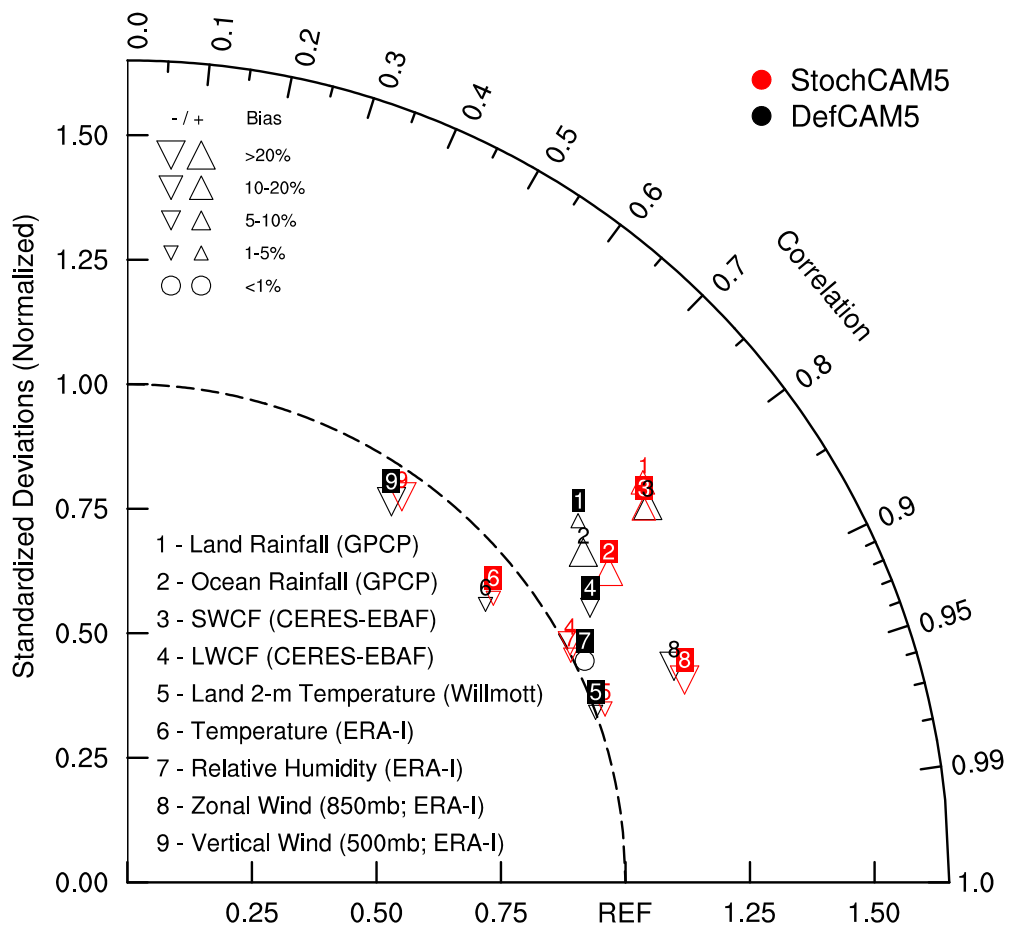
799
800

Figures



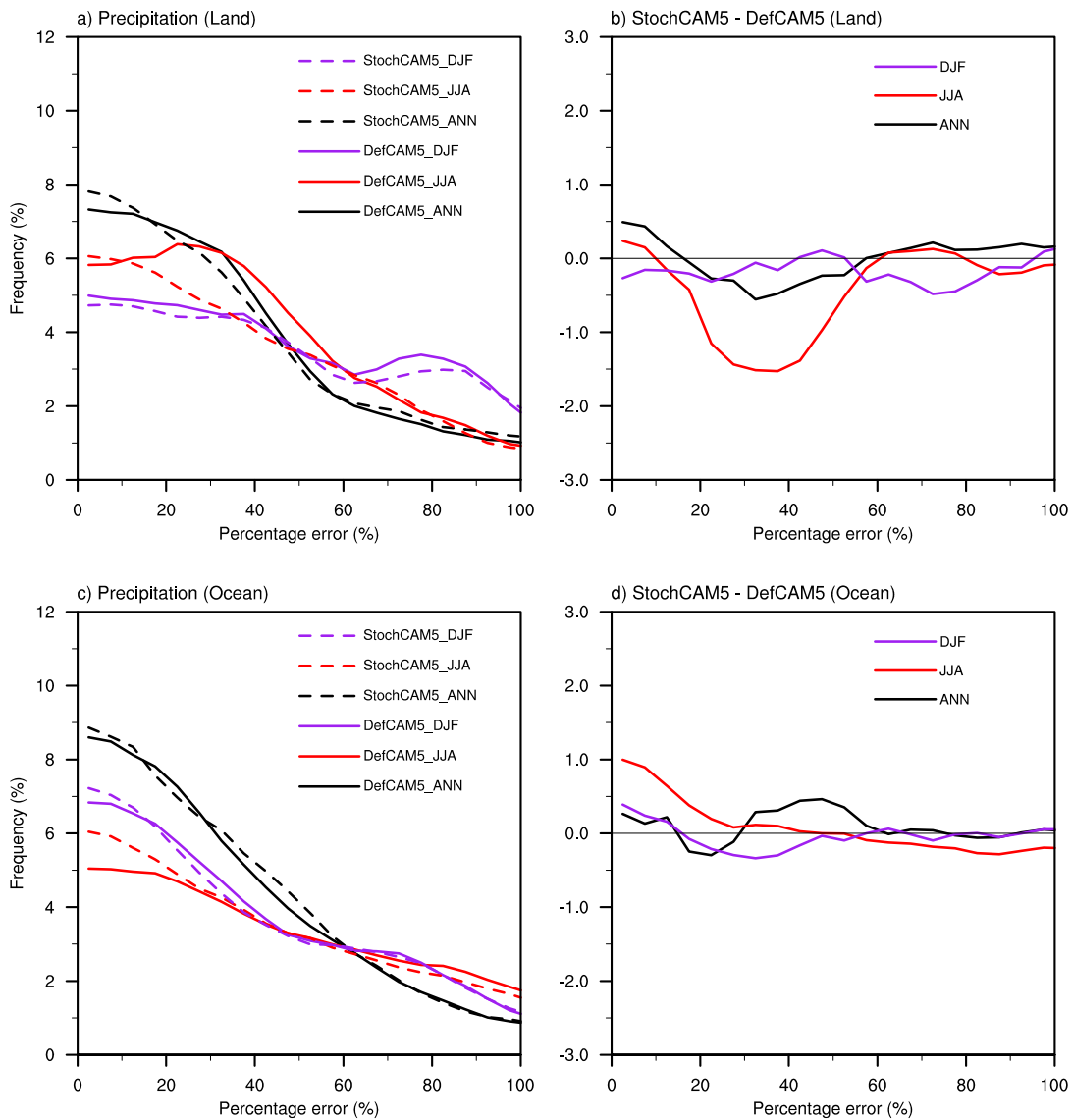
801
802
803
804
805
806
807

Figure 1: Structure of the stochastic entrainment rate implemented in the ZMNR deep convection scheme. Entrainment rate (ε) from the parcel launch level to lifting condensation level (LCL) is kept the same as default value $\varepsilon(\Delta z) = 0.1 \times 10^{-3} \text{ m}^{-1}$. Entrainment above LCL is stochastically computed until the level of neutral buoyancy (LNB). The levels used here are the default model levels and the distance Δz is the difference between the two model levels .

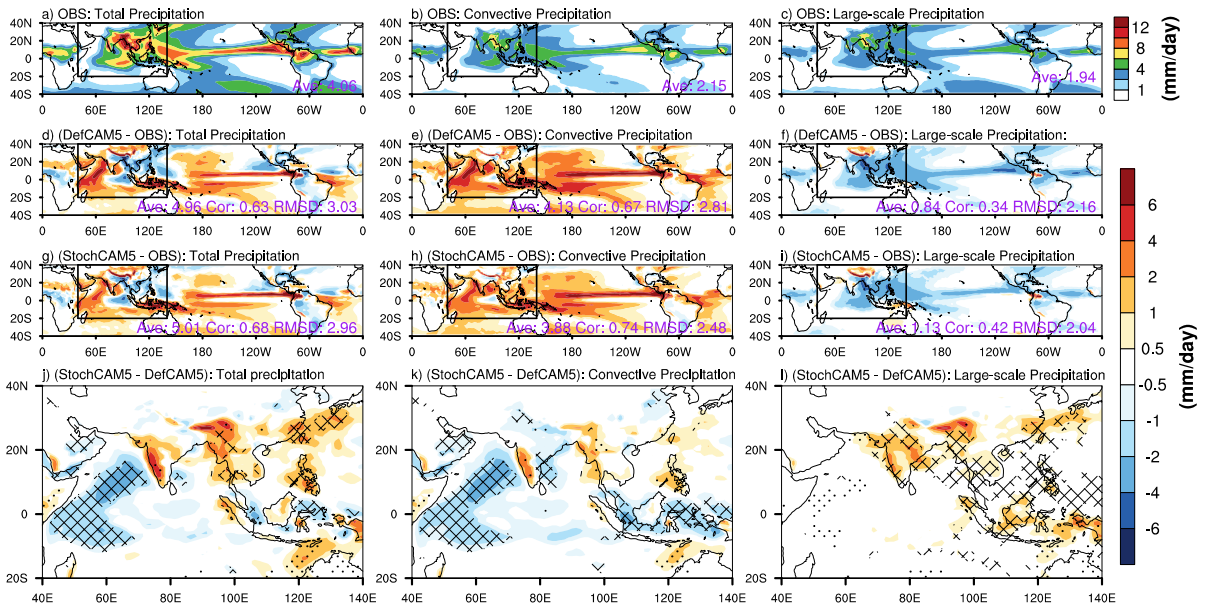


808 **Figure 2:** Taylor diagram with metrics for DefCAM5 and StochCAM5 over the tropics (30°S-
 809 30°N). The specific humidity (point 6) and temperature (point 7) are the mass-weighted vertical
 810 average from 1000-100 hPa. The four metrics used here are the Pearson correlation coefficient
 811 (represented by the cosine of the angle from the horizontal axis), the centered root mean square
 812 error (represented by the distance from the point on the horizontal axis defined as the reference
 813 point or REF), the normalized standard deviation (represented by the radial distance from the
 814 origin), and the percentage error (represented by the size of markers).

815
816

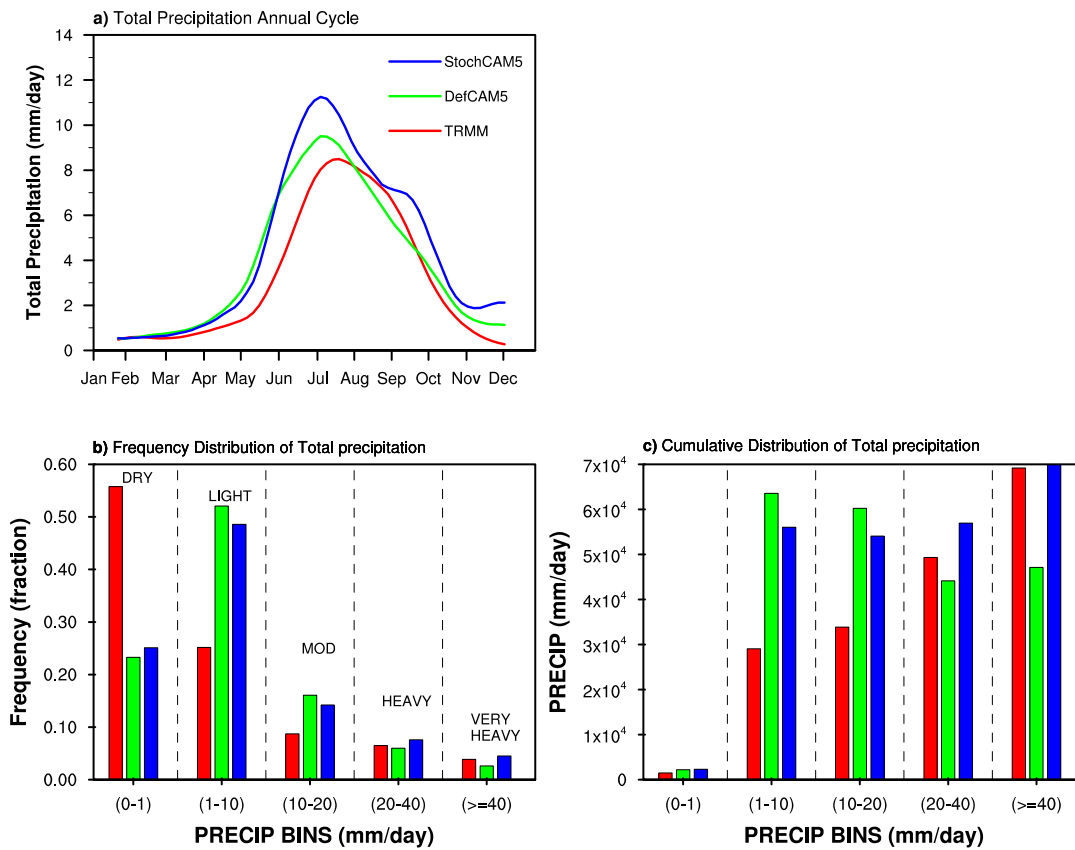


817 **Figure 3:** The frequency distribution of percentage bias for annual and seasonal (JJA and DJF)
 818 mean precipitation over the tropical land and ocean (30°S-30°N) from DefCAM5 and
 819 StochCAM5, as well as their differences. The 5% bin interval is used in computing the frequency
 820 of percentage bias.

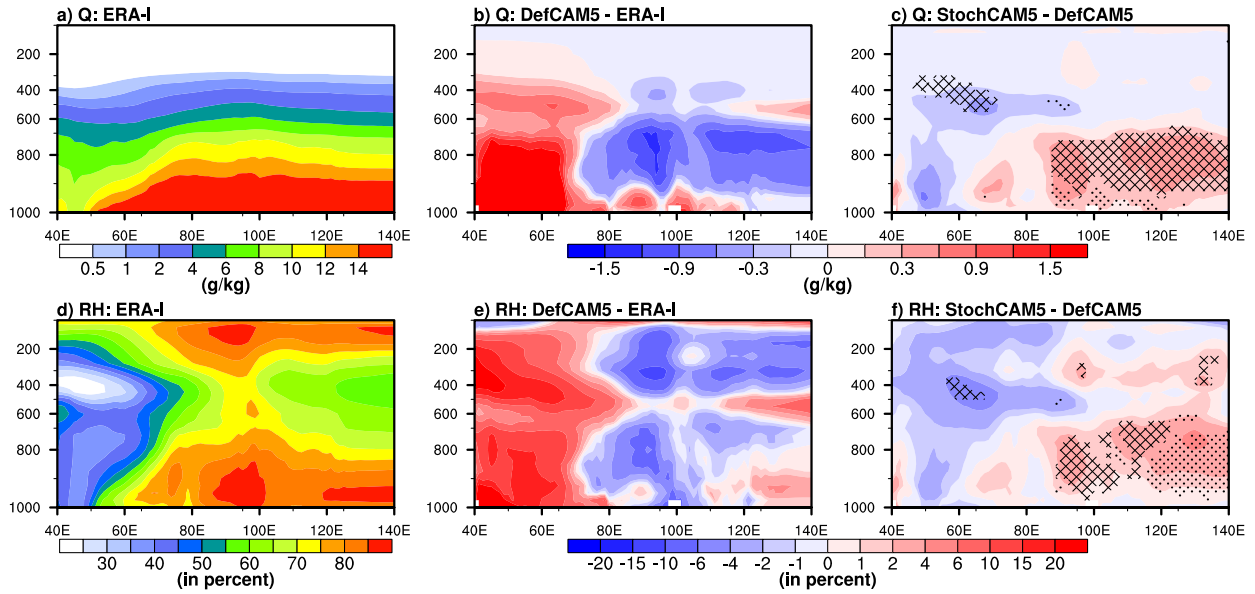


821 **Figure 4:** Spatial variation of JJAS mean precipitation. **a-c** shows the JJAS mean **(a)** total
 822 precipitation, **(b)** convective precipitation and **(c)** large-scale precipitation from GPCP observations
 823 over the tropics. **d-f** and **g-i** shows the difference in total, convective, and large-scale precipitation
 824 for DefCAM5 and StochCAM5 with respect to observations, respectively over the tropics. **j-l**
 825 shows the difference in total, convective, and large-scale precipitation for StochCAM5 with
 826 respect to DefCAM5 over South Asia (the zoomed region in black rectangle). The average value
 827 (Ave.), correlation (Corr.), and the root mean square difference (RMSD) for precipitation over
 828 South Asia are also shown at the bottom of a-i. Hatching (stippling) shows the differences which
 829 are improved (deteriorated) at 95% confidence level (two-tailed student t-test) in StochCAM5 with
 830 respect to DefCAM5.

831



832 **Figure 5:** (a) annual total precipitation cycle, (b) frequency distribution of daily precipitation rate
833 over the Indian land during JJAS, and c) amount of precipitation falling in each bin of precipitation
834 rate over the Indian land during JJAS.
835

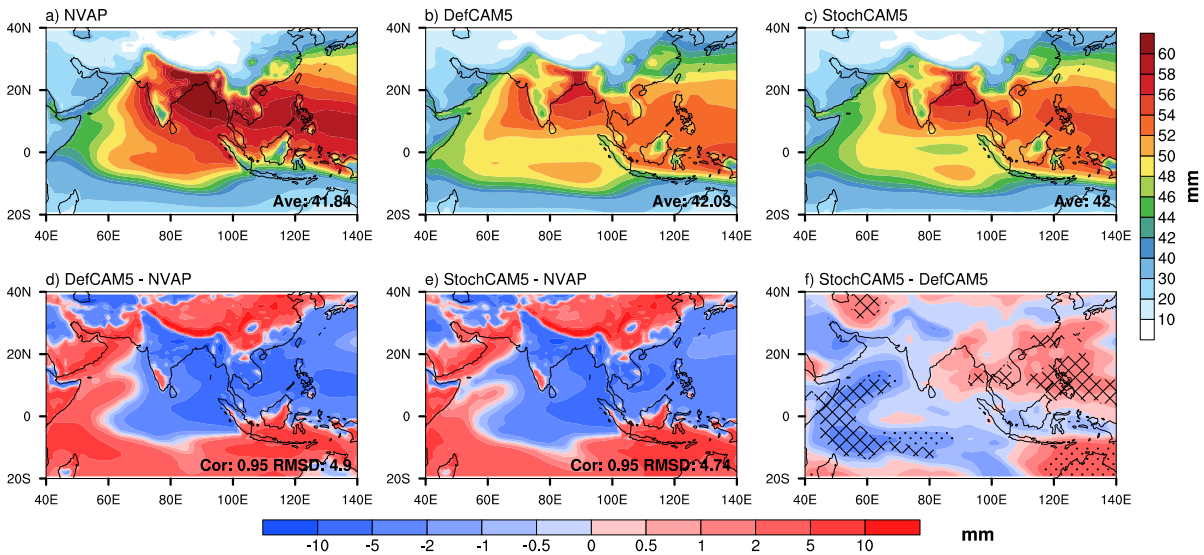


836

837 Figure 6: The JJAS meridional mean cross sections of (a-c) specific humidity and (d-f) relative
 838 humidity in belt of Indian latitudes (0° - 30° N) for (a, d) ERA-I, (b, e) DefCAM5 -ERA-I, and (c,
 839 f) StochCAM5 –DefCAM5. Hatching (stippling) shows the differences which are improved
 840 (deteriorated) at 95% confidence level in StochCAM5 with respect to DefCAM5. Q – specific
 841 humidity; RH – relative humidity.

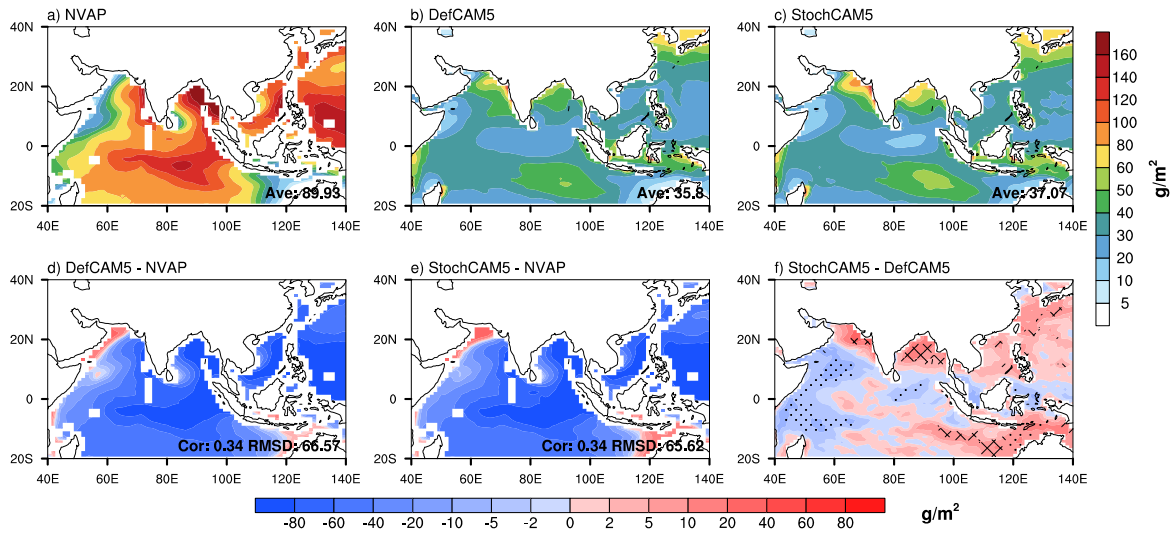
842

843

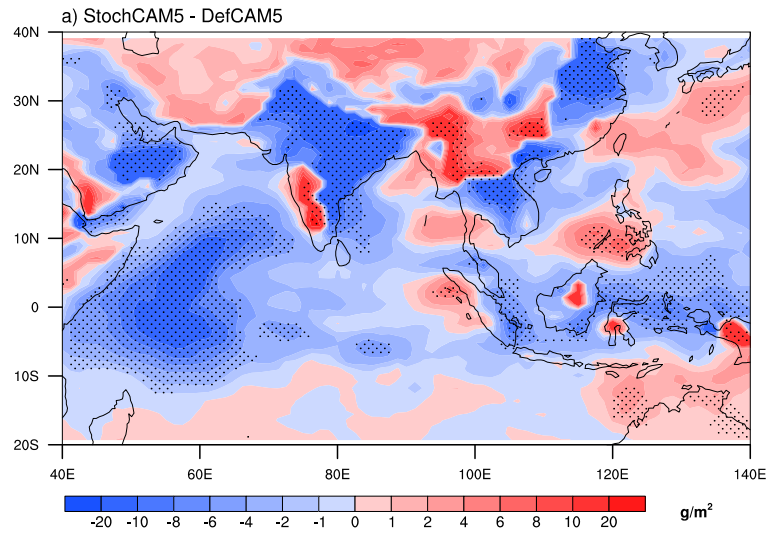


844

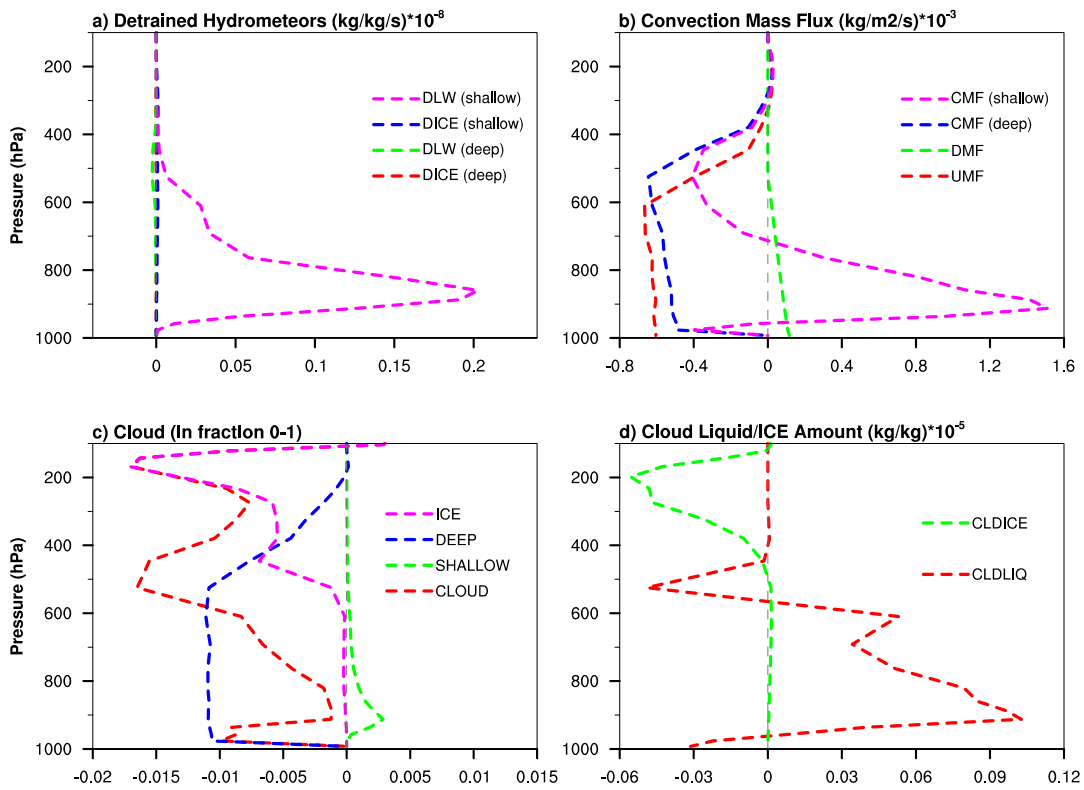
845 Figure 7: JJAS mean total column water vapor over South Asia for (a) NVAP, (b) DefCAM5, and
 846 (c) StochCAM5 as well as their differences for (d) DefCAM5 – NVAP, (e) StochCAM5 – NVAP,
 847 and (f) StochCAM5 - DefCAM5. Hatching (stippling) shows the differences which are improved
 848 (deteriorated) at 95% confidence level in StochCAM5 with respect to DefCAM5. NVAP -
 849 National Aeronautics and Space Administration (NASA) Water Vapor Project.
 850



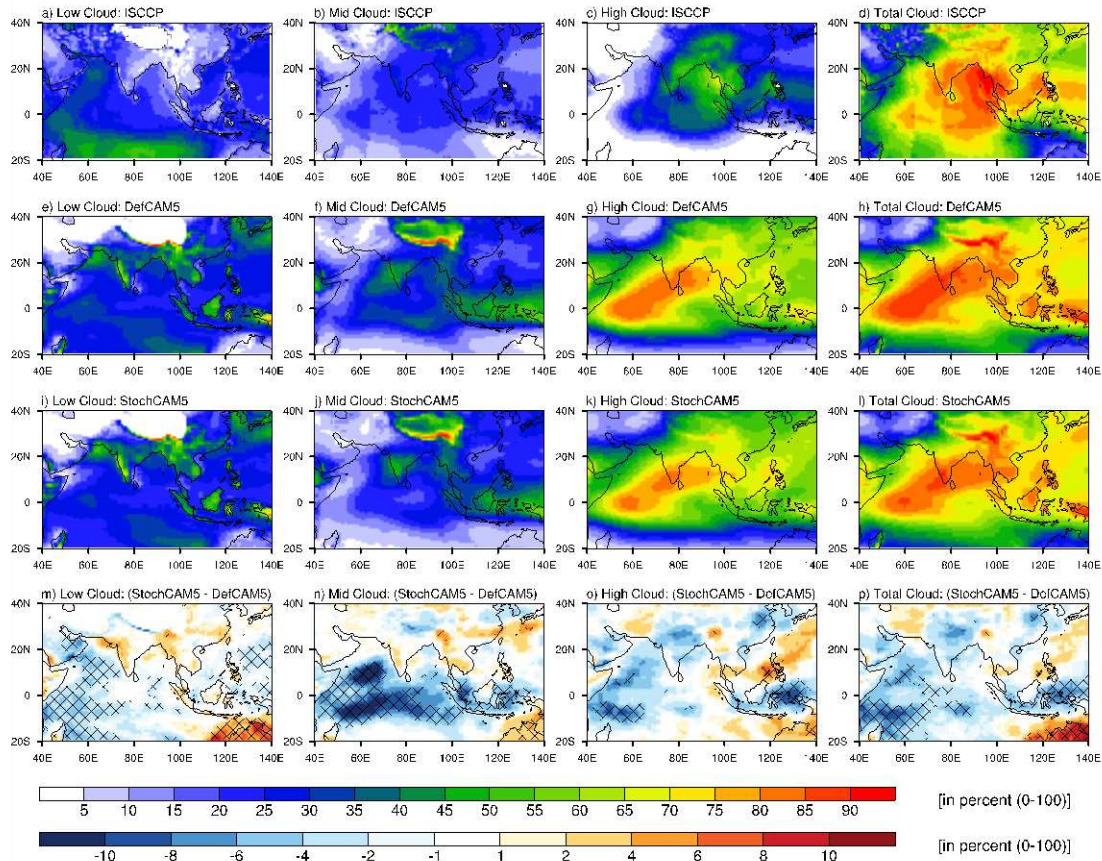
851
 852 Figure 8: JJAS mean total liquid water path (LWP) over South Asia for (a) NVAP, (b) DefCAM5,
 853 and (c) StochCAM5 as well as their differences for (d) DefCAM5 – NVAP, (e) StochCAM5 –
 854 NVAP, and (f) StochCAM5 - DefCAM5. Hatching (stippling) shows the differences which are
 855 improved (deteriorated) at 95% confidence level in StochCAM5 with respect to DefCAM5.
 856



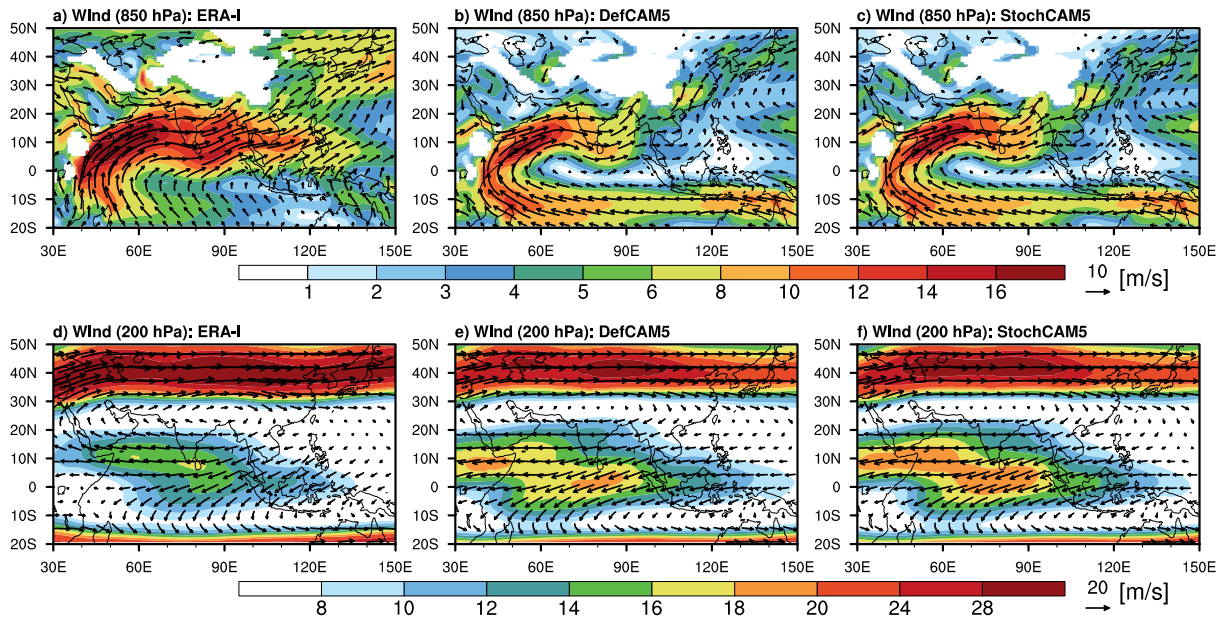
857
 858 **Figure 9:** JJAS mean difference of ice water path (IWP) over South Asia between StochCAM5
 859 and DefCAM5. The stippled regions show the differences which are significant at 95% confidence
 860 level.
 861



863 **Figure 10:** JJAS mean difference of (a) detrained liquid water (DLW) and detrained ice (DICE)
 864 from deep and shallow convection, (b) updraft mass flux (UMF), downdraft mass flux (DMF),
 865 convective mass flux (CMF) for shallow and deep convection, (c) cloud cover distribution of ice,
 866 deep, shallow, and total cloud, and (d) cloud liquid and cloud ice amount over South Asia.
 867



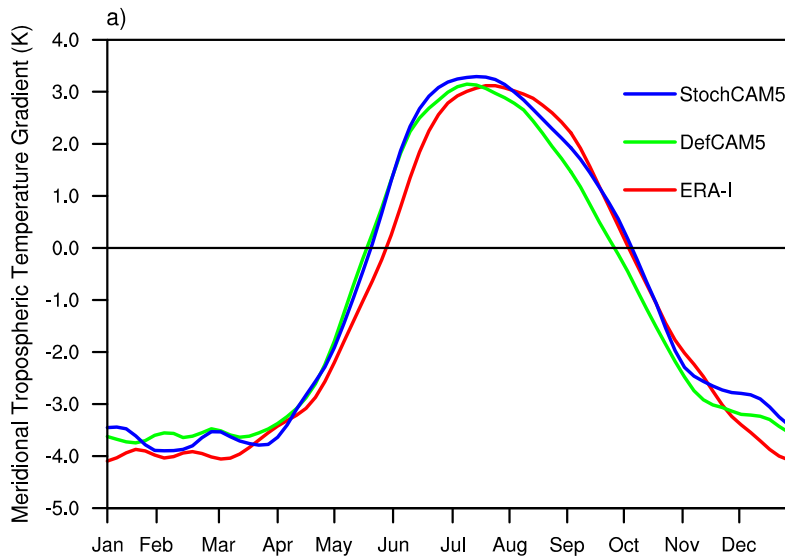
868
 869 **Figure 11:** JJAS mean low, middle, high, and total cloud cover distribution over South Asia for
 870 (a-d) ISCCP, (e-h) DefCAM5, and (i-l) StochCAM5, as well as the difference for (m-p)
 871 StochCAM5 - DefCAM5. Hatching (stippling) shows the differences which are improved
 872 (deteriorated) at 95% confidence level in StochCAM5 with respect to DefCAM5. ISCCP -
 873 International Satellite Cloud Climatology Project.



874

875 **Figure 12:** JJAS mean (a-c) low-level wind at 850 hPa and (d-f) upper-level wind at 200 hPa for
 876 (a, d) ERA-I, (b, e) DefCAM5, and (c, f) StochCAM5.

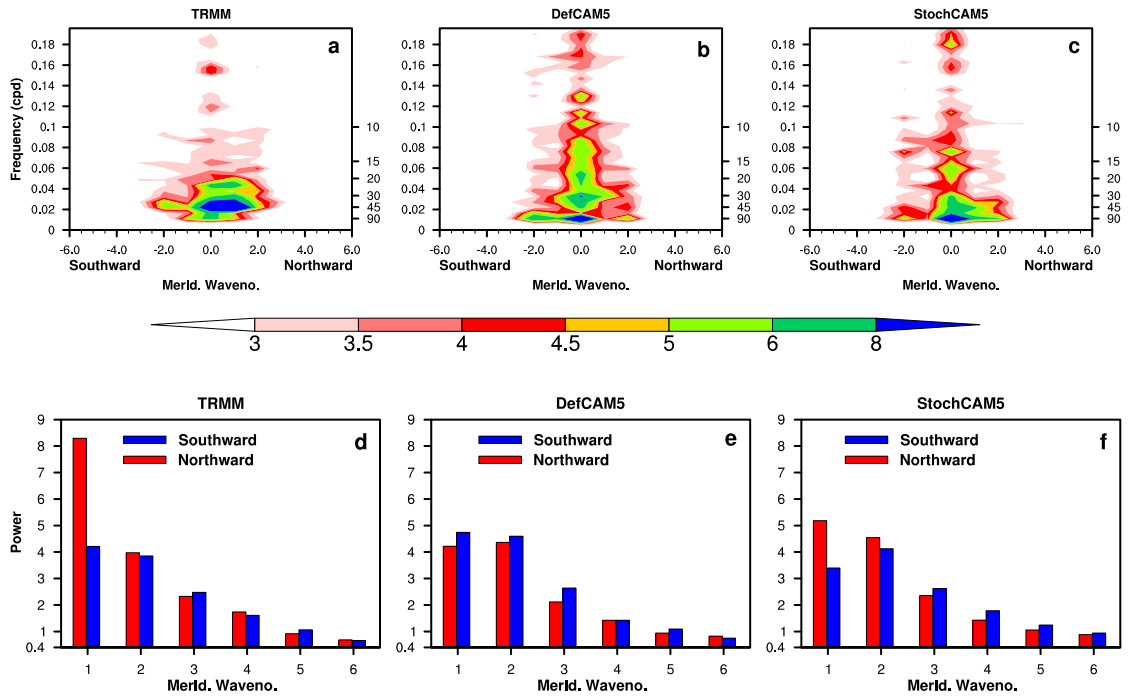
877



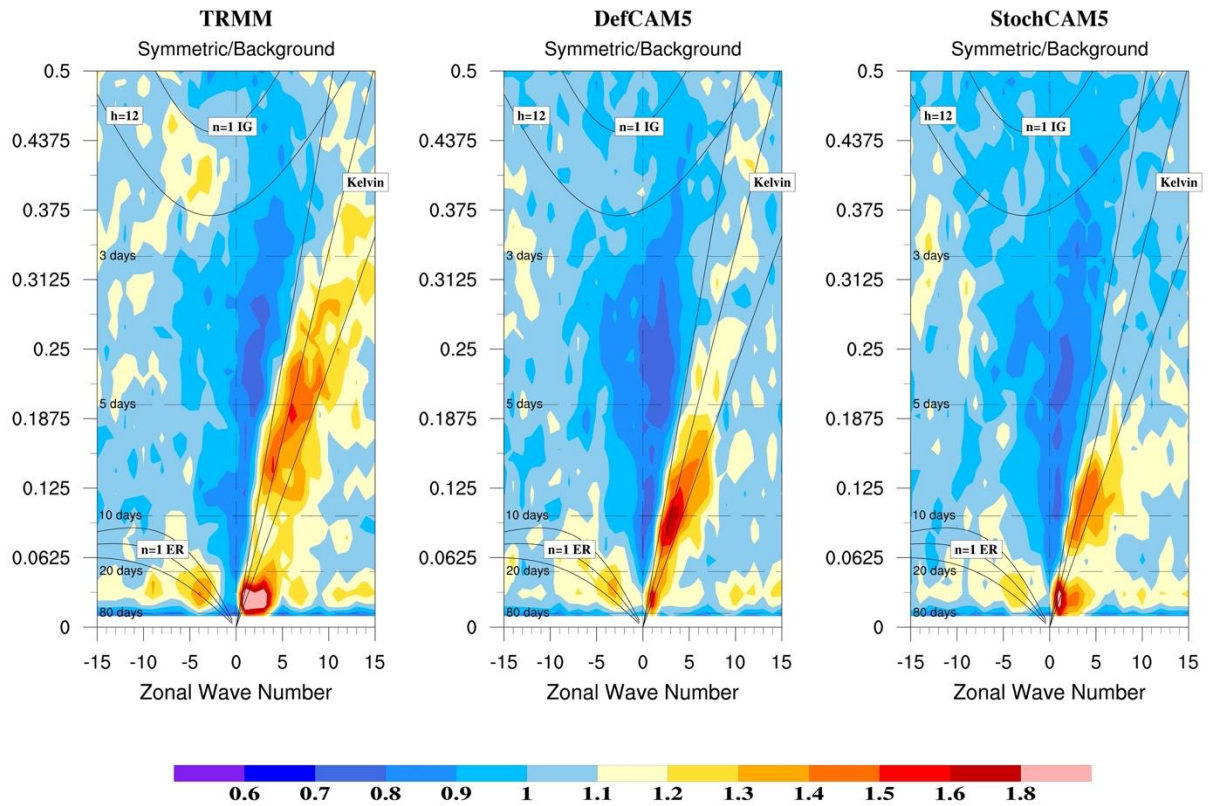
878

879 **Figure 13:** The annual cycle of meridional tropospheric temperature gradient (MTTG) for ERA-I
 880 (red), DefCAM5 (green), and StochCAM5 (blue). MTTG is estimated by taking the difference of
 881 vertically averaged (600-200 hPa) temperature between the two boxes – one over 5°-35°N and
 882 40°-100°E and other over 5°N-15°S and 40-100°E. MTTG also defines the monsoon onset date

883 when this changes the sign from negative to positive on the annual cycle and the vice-versa for the
 884 monsoon withdrawal.
 885



886
 887 **Figure 14:** The north-south wavenumber-frequency spectra of precipitation during JJAS for (a)
 888 TRMM, (b) DefCAM5, and (c) StochCAM5 over the domain of 15°S-30°N and 60°-95°E. The
 889 power of precipitation spectrum separated as the northward and southward component, which is
 890 calculated from the north-south wavenumber-frequency spectra of precipitation averaged over 30-
 891 90 days period for (d) TRMM, (e) DefCAM5, and (f) StochCAM5.
 892



893

894 **Figure 15:** The symmetric component of Wheeler-Kiladis space-time power spectrum for (a)

895 TRMM, (b) DefCAM5, and (c) StochCAM5. It is computed from the daily time-series of total

896 precipitation in the global belt of equatorial region (15°N-15°S) during JJAS.

897

Figures

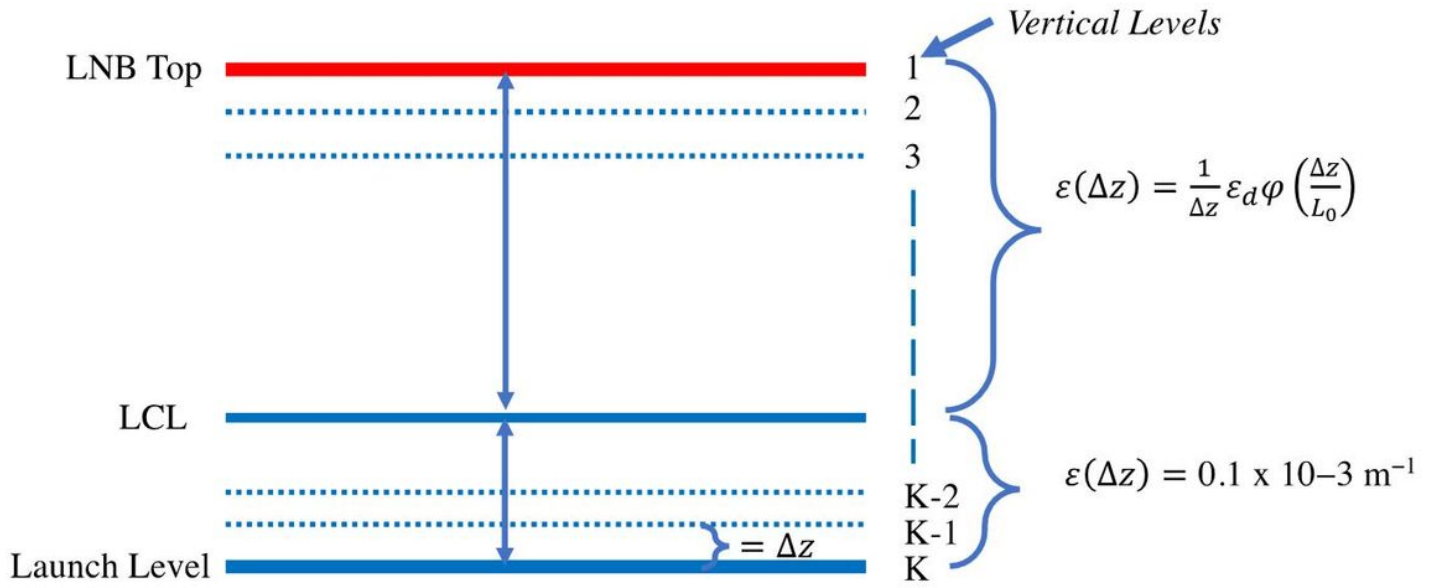


Figure 1

Structure of the stochastic entrainment rate implemented in the ZMNR deep convection scheme. Entrainment rate (ϵ) from the parcel launch level to lifting condensation level (LCL) is kept the same as default value $\epsilon(\Delta z) = 0.1 \times 10^{-3} \text{ m}^{-1}$. Entrainment above LCL is stochastically computed until the level of neutral buoyancy (LNB). The levels used here are the default model levels and the distance Δz is the difference between the two model levels.

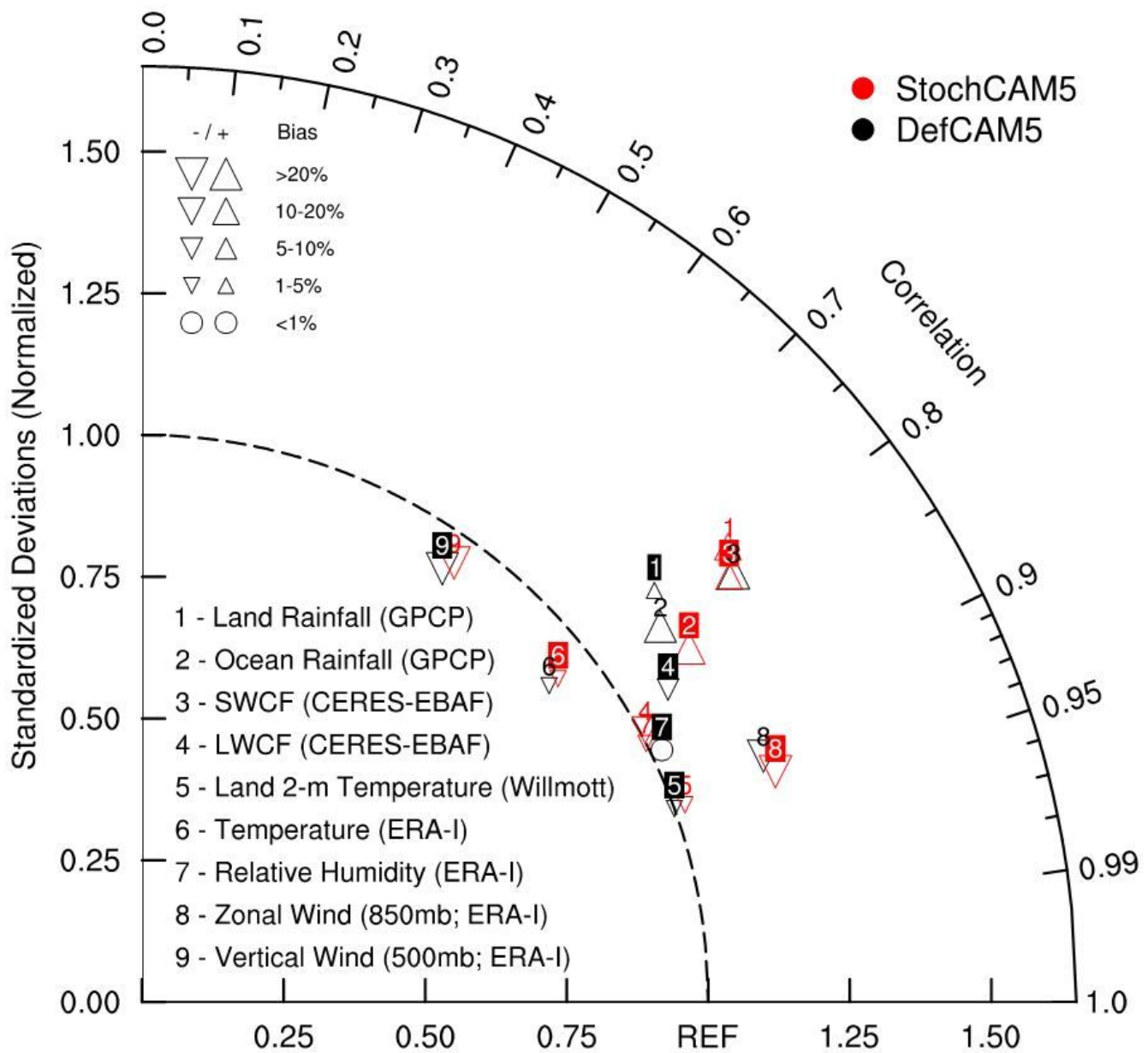


Figure 2

Taylor diagram with metrics for DefCAM5 and StochCAM5 over the tropics (30°S-30°N). The specific humidity (point 6) and temperature (point 7) are the mass-weighted vertical average from 1000-100 hPa. The four metrics used here are the Pearson correlation coefficient (represented by the cosine of the angle from the horizontal axis), the centered root mean square error (represented by the distance from the point on the horizontal axis defined as the reference point or REF), the normalized standard deviation (represented by the radial distance from the origin), and the percentage error (represented by the size of markers).

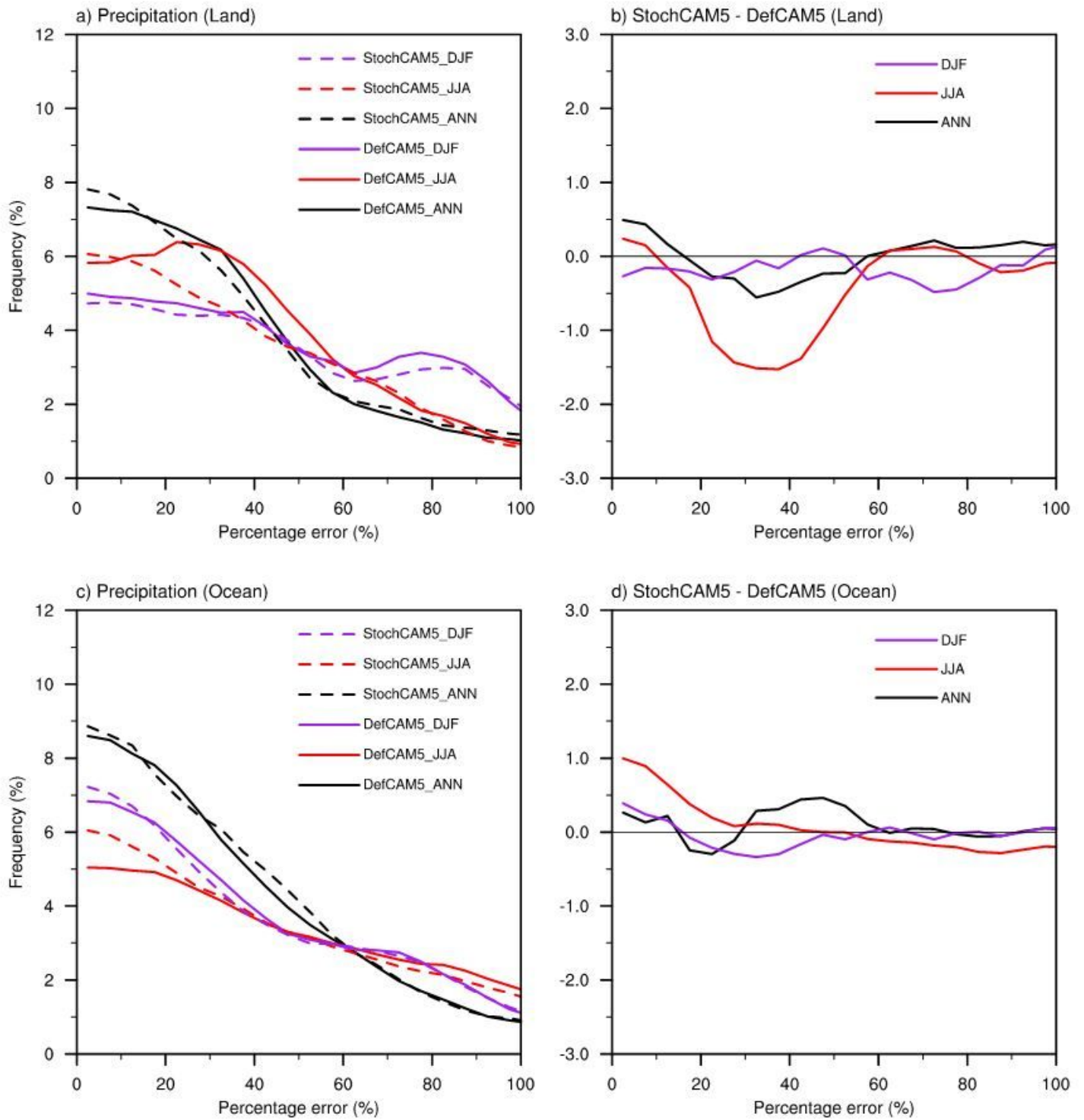


Figure 3

The frequency distribution of percentage bias for annual and seasonal (JJA and DJF) mean precipitation over the tropical land and ocean (30°S-30°N) from DefCAM5 and StochCAM5, as well as their differences. The 5% bin interval is used in computing the frequency of percentage bias.

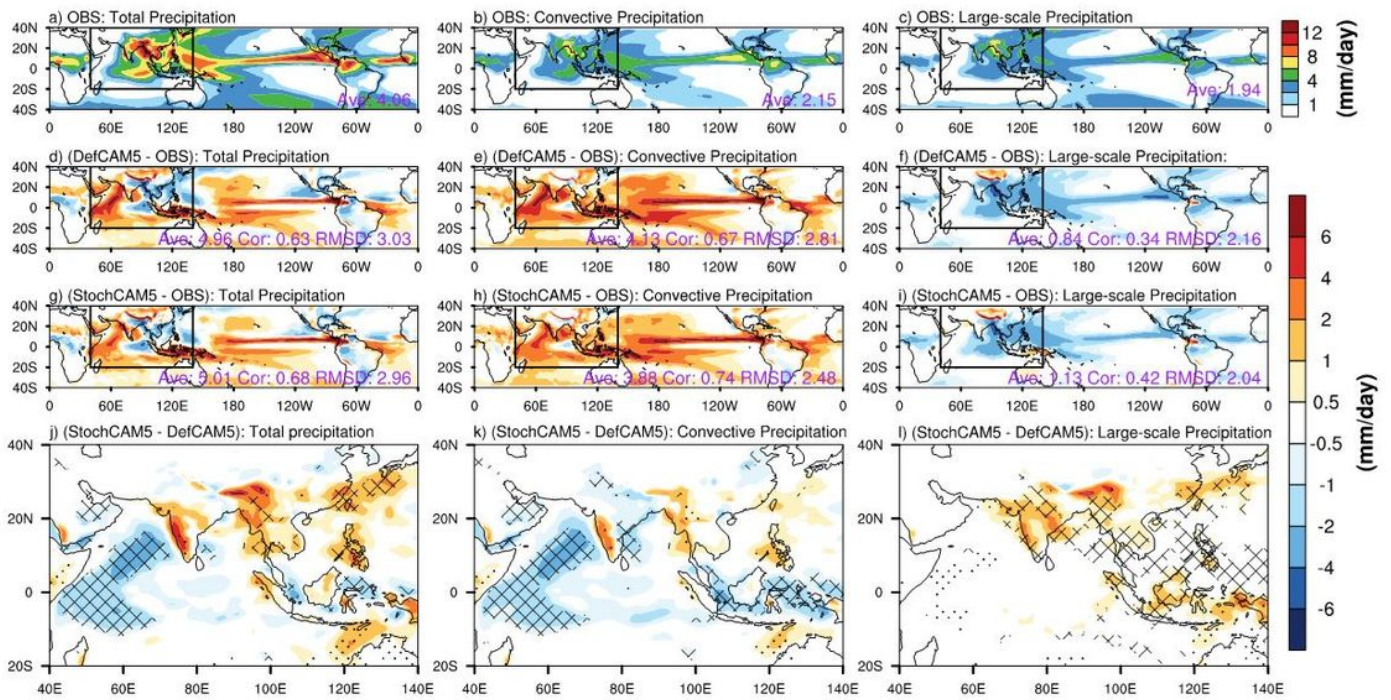


Figure 4

Spatial variation of JJAS mean precipitation. a-c shows the JJAS mean (a) total precipitation, (b) convective precipitation and c) large-scale precipitation from GPCP observations over the tropics. d-f and g-i shows the difference in total, convective, and large-scale precipitation for DefCAM5 and StochCAM5 with respect to observations, respectively over the tropics. j-l shows the difference in total, convective, and large-scale precipitation for StochCAM5 with respect to DefCAM5 over South Asia (the zoomed region in black rectangle). The average value (Ave.), correlation (Corr.), and the root mean square difference (RMSD) for precipitation over South Asia are also shown at the bottom of a-i. Hatching (stippling) shows the differences which are improved (deteriorated) at 95% confidence level (two-tailed student t-test) in StochCAM5 with respect to DefCAM5. Note: The designations employed and the presentation of the material on this map do not imply the expression of any opinion whatsoever on the part of Research Square concerning the legal status of any country, territory, city or area or of its authorities, or concerning the delimitation of its frontiers or boundaries. This map has been provided by the authors.

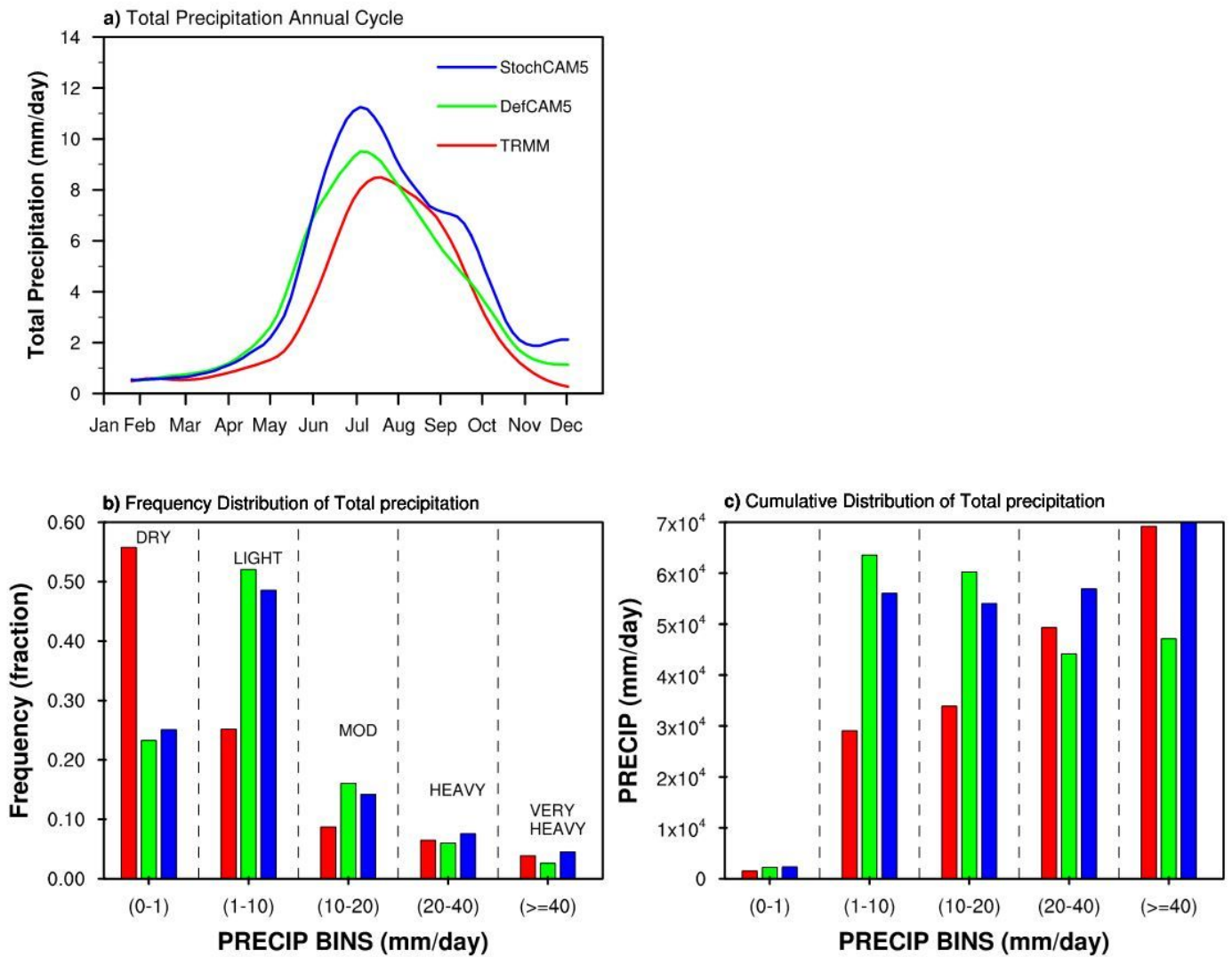


Figure 5

(a) annual total precipitation cycle, (b) frequency distribution of daily precipitation rate over the Indian land during JJAS, and c) amount of precipitation falling in each bin of precipitation rate over the Indian land during JJAS.

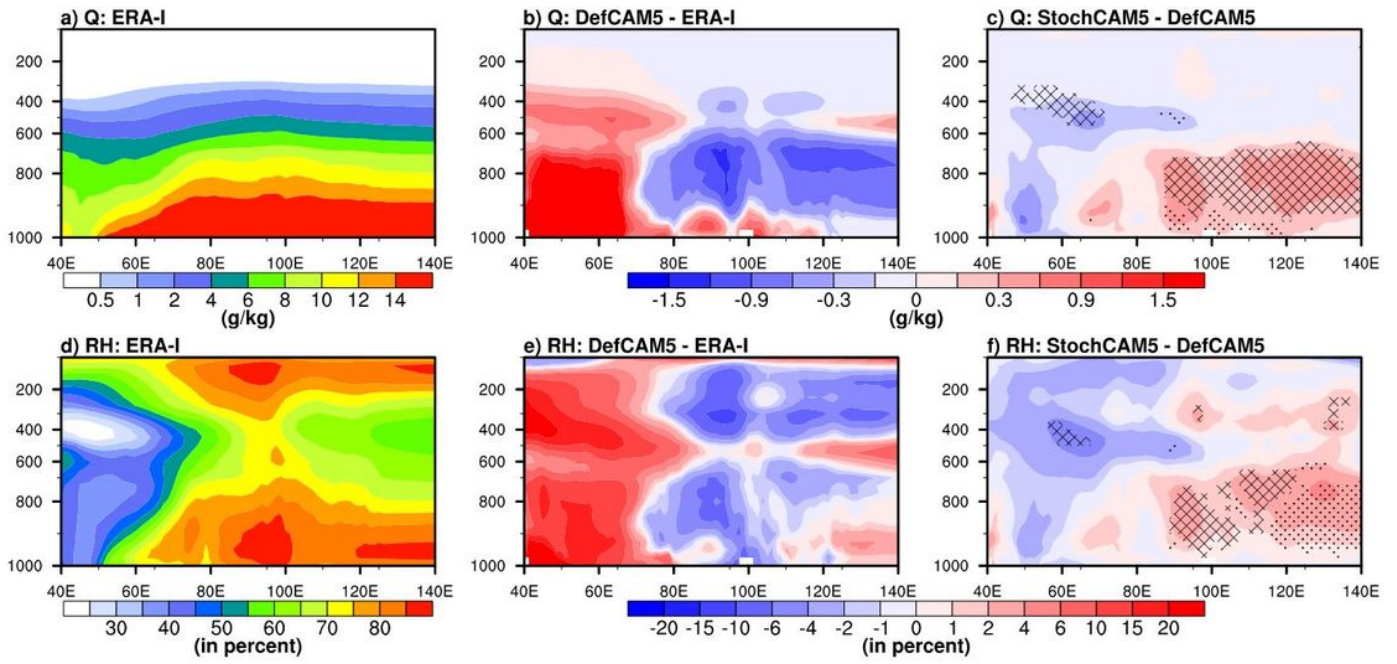


Figure 6

The JJAS meridional mean cross sections of (a-c) specific humidity and (d-f) relative humidity in belt of Indian latitudes (0° - 30° N) for (a, d) ERA-I, (b, e) DefCAM5 -ERA-I, and (c, f) StochCAM5 –DefCAM5. Hatching (stippling) shows the differences which are improved (deteriorated) at 95% confidence level in StochCAM5 with respect to DefCAM5. Q – specific humidity; RH – relative humidity.

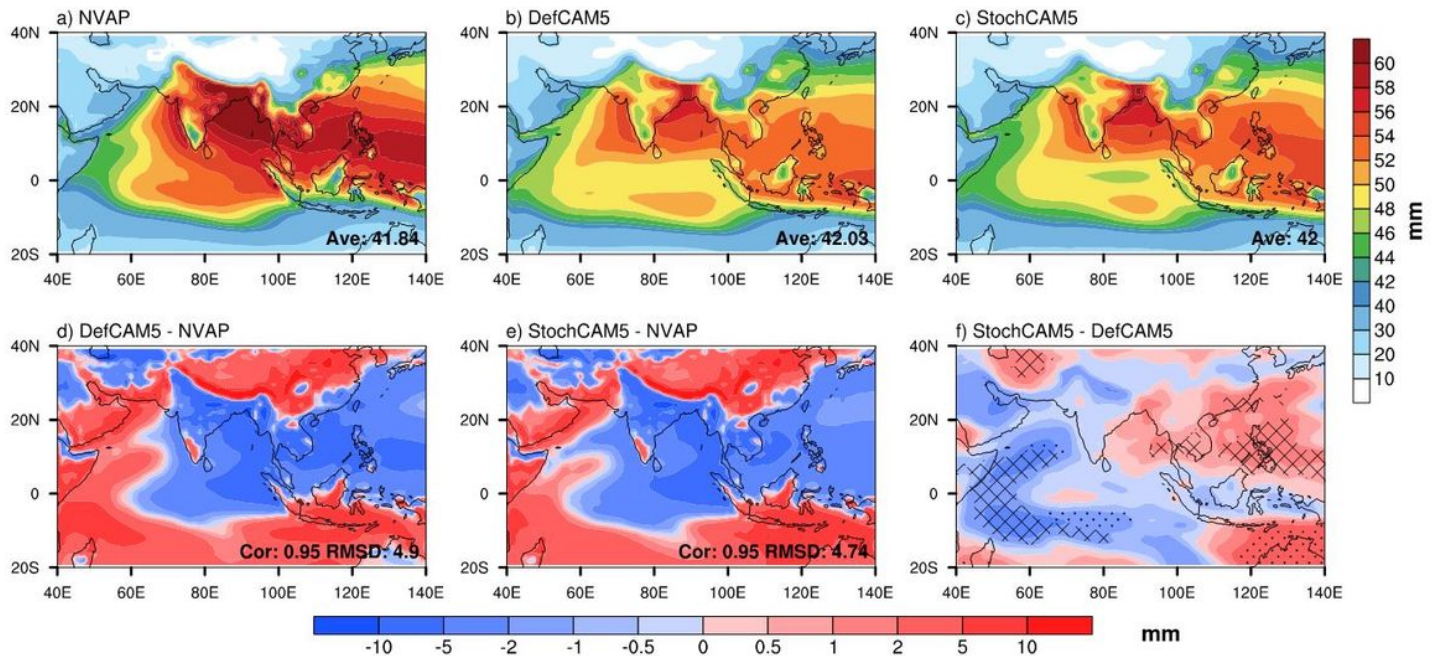


Figure 7

JJAS mean total column water vapor over South Asia for (a) NVAP, (b) DefCAM5, and (c) StochCAM5 as well as their differences for (d) DefCAM5 – NVAP, (e) StochCAM5 – NVAP, and (f) StochCAM5 - DefCAM5. Hatching (stippling) shows the differences which are improved (deteriorated) at 95% confidence level in StochCAM5 with respect to DefCAM5. NVAP - National Aeronautics and Space Administration (NASA) Water Vapor Project. Note: The designations employed and the presentation of the material on this map do not imply the expression of any opinion whatsoever on the part of Research Square concerning the legal status of any country, territory, city or area or of its authorities, or concerning the delimitation of its frontiers or boundaries. This map has been provided by the authors.

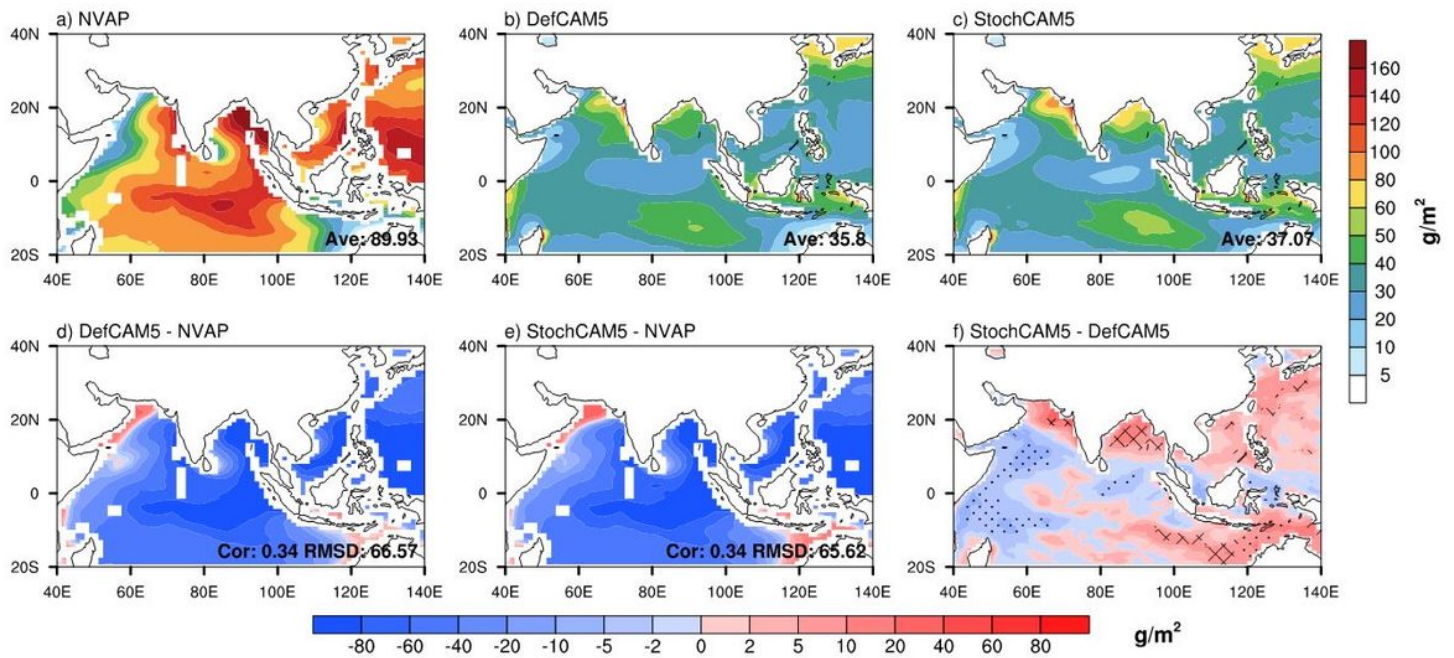


Figure 8

JJAS mean total liquid water path (LWP) over South Asia for (a) NVAP, (b) DefCAM5, and (c) StochCAM5 as well as their differences for (d) DefCAM5 – NVAP, (e) StochCAM5 – NVAP, and (f) StochCAM5 - DefCAM5. Hatching (stippling) shows the differences which are improved (deteriorated) at 95% confidence level in StochCAM5 with respect to DefCAM5. Note: The designations employed and the presentation of the material on this map do not imply the expression of any opinion whatsoever on the part of Research Square concerning the legal status of any country, territory, city or area or of its authorities, or concerning the delimitation of its frontiers or boundaries. This map has been provided by the authors.

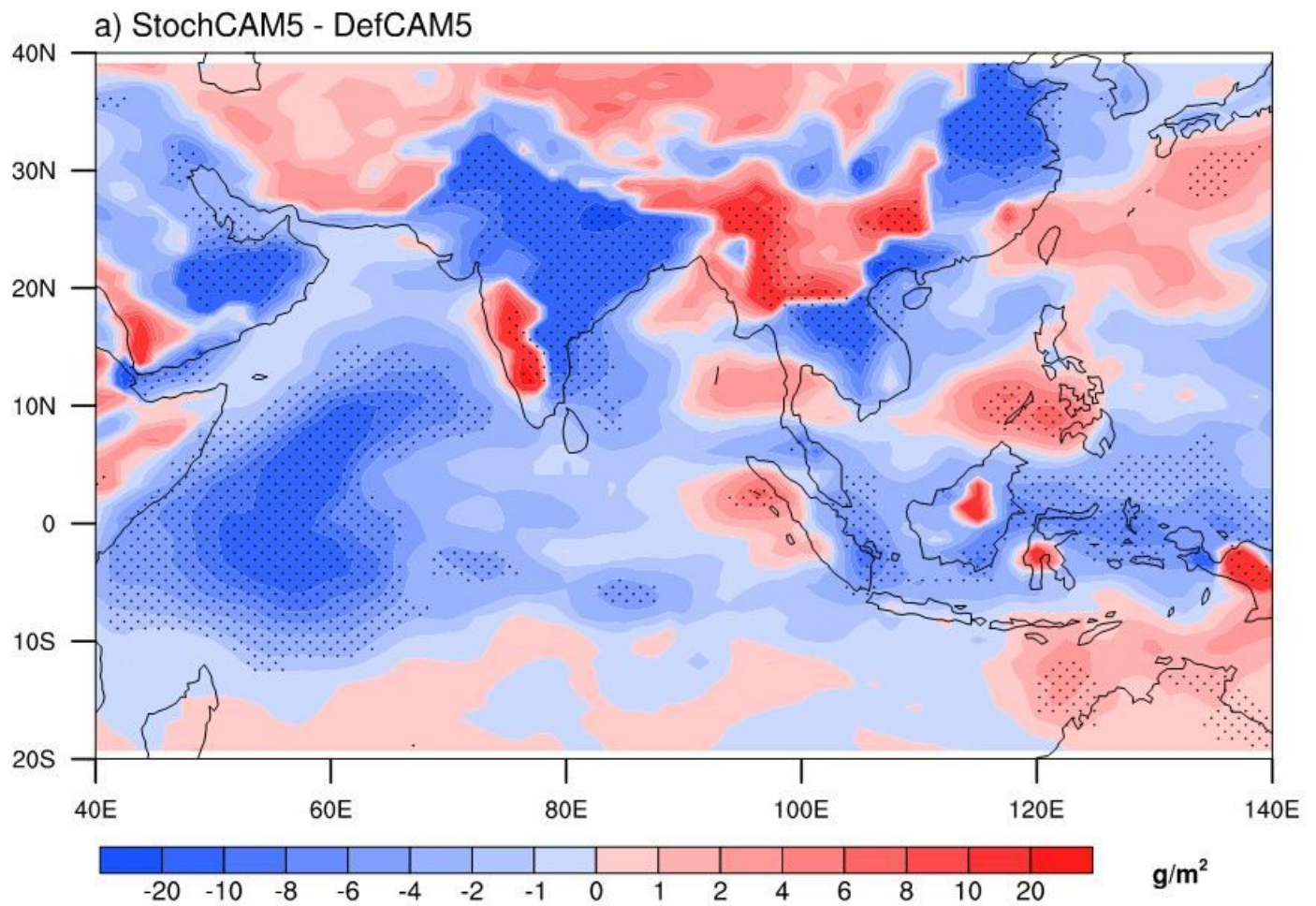


Figure 9

JJAS mean difference of ice water path (IWP) over South Asia between StochCAM5 and DefCAM5. The stippled regions show the differences which are significant at 95% confidence level. Note: The designations employed and the presentation of the material on this map do not imply the expression of any opinion whatsoever on the part of Research Square concerning the legal status of any country, territory, city or area or of its authorities, or concerning the delimitation of its frontiers or boundaries. This map has been provided by the authors.

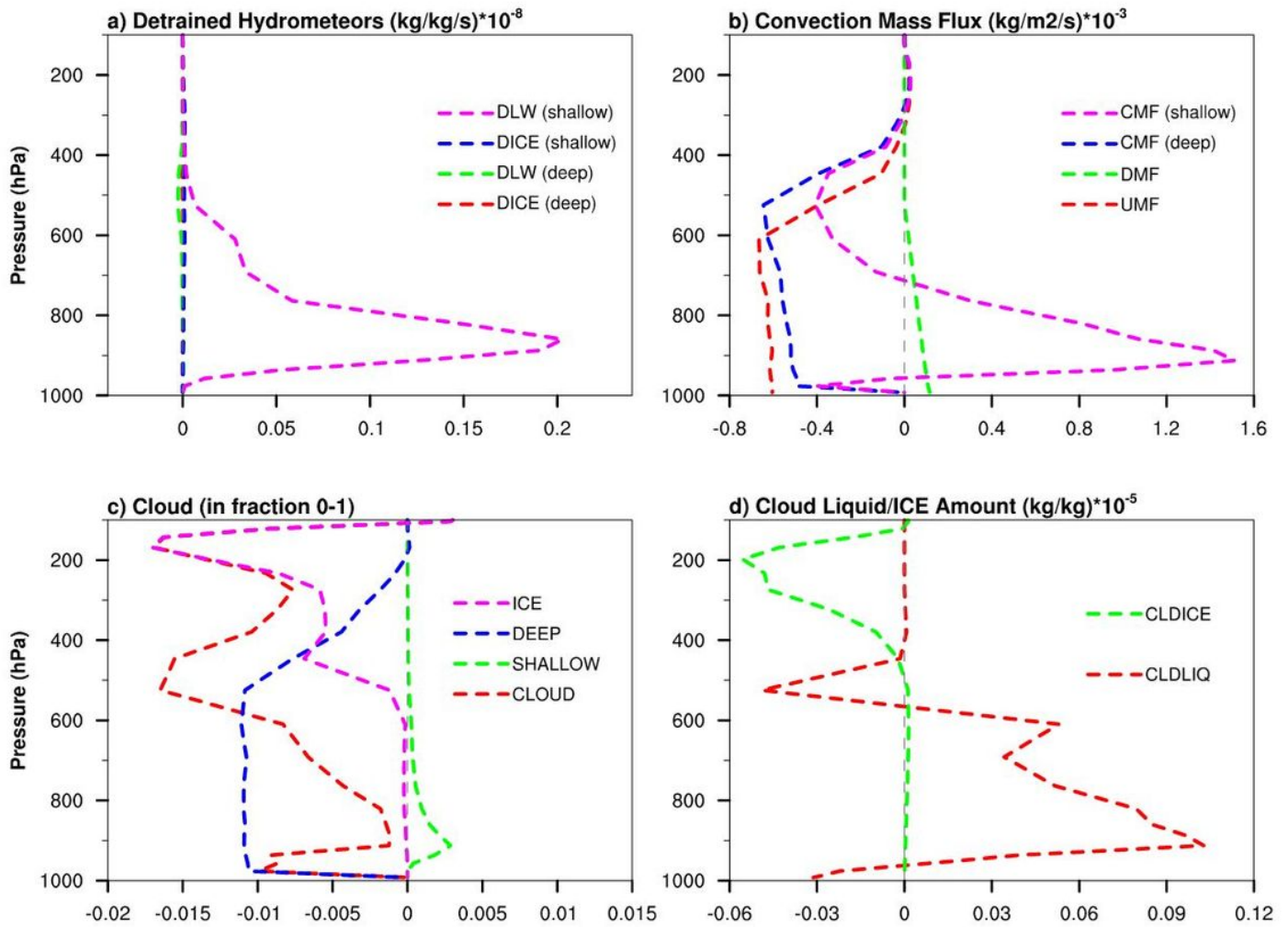


Figure 10

JJAS mean difference of (a) detrained liquid water (DLW) and detrained ice (DICE) from deep and shallow convection, (b) updraft mass flux (UMF), downdraft mass flux (DMF), convective mass flux (CMF) for shallow and deep convection, (c) cloud cover distribution of ice, deep, shallow, and total cloud, and (d) cloud liquid and cloud ice amount over South Asia.

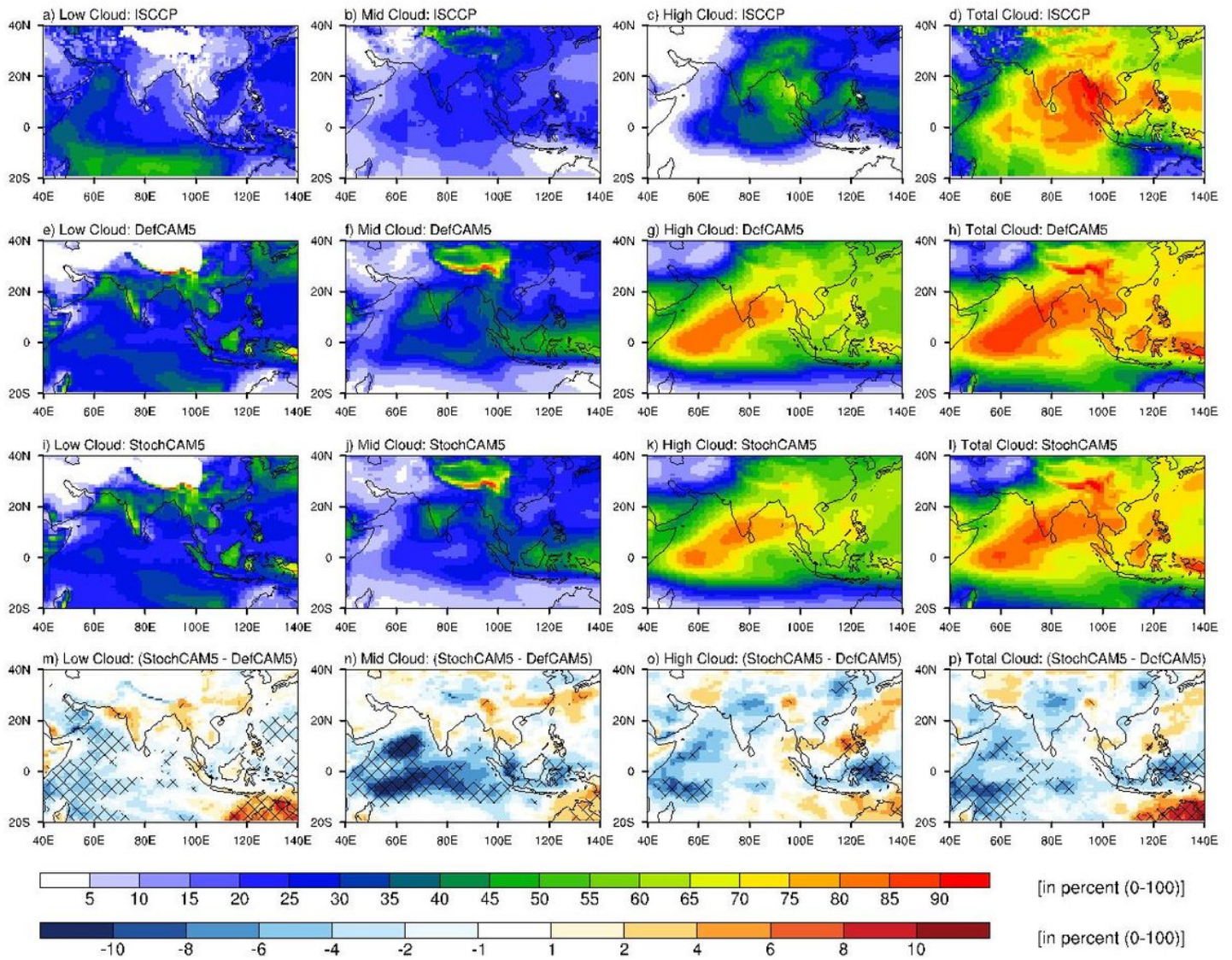


Figure 11

JJAS mean low, middle, high, and total cloud cover distribution over South Asia for (a-d) ISCCP, (e-h) DefCAM5, and (i-l) StochCAM5, as well as the difference for (m-p) StochCAM5 - DefCAM5. Hatching (stippling) shows the differences which are improved (deteriorated) at 95% confidence level in StochCAM5 with respect to DefCAM5. ISCCP - International Satellite Cloud Climatology Project. Note: The designations employed and the presentation of the material on this map do not imply the expression of any opinion whatsoever on the part of Research Square concerning the legal status of any country, territory, city or area or of its authorities, or concerning the delimitation of its frontiers or boundaries. This map has been provided by the authors.

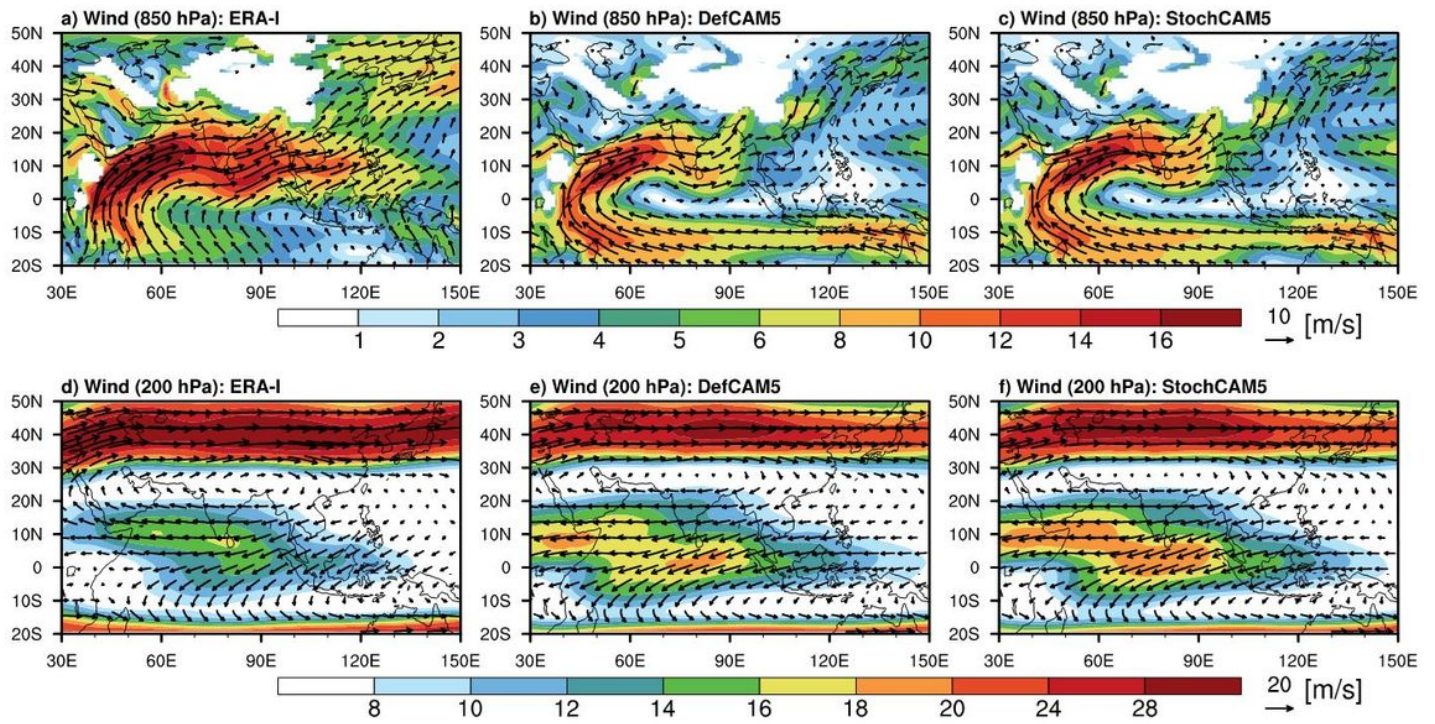


Figure 12

JJAS mean (a-c) low-level wind at 850 hPa and (d-f) upper-level wind at 200 hPa for (a, d) ERA-I, (b, e) DefCAM5, and (c, f) StochCAM5. Note: The designations employed and the presentation of the material on this map do not imply the expression of any opinion whatsoever on the part of Research Square concerning the legal status of any country, territory, city or area or of its authorities, or concerning the delimitation of its frontiers or boundaries. This map has been provided by the authors.

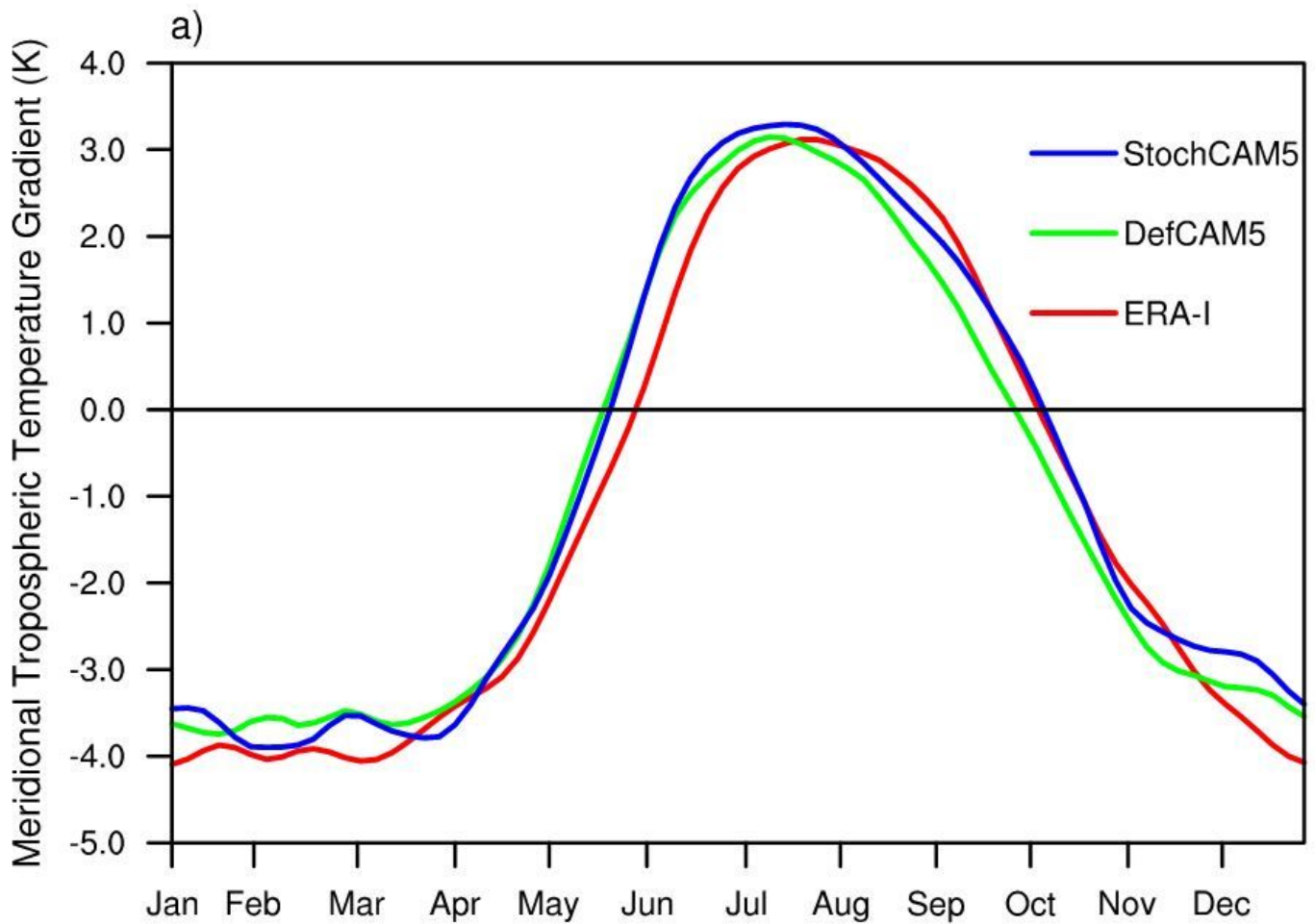


Figure 13

The annual cycle of meridional tropospheric temperature gradient (MTTG) for ERA-I (red), DefCAM5 (green), and StochCAM5 (blue). MTTG is estimated by taking the difference of vertically averaged (600-200 hPa) temperature between the two boxes – one over 5°-35°N and 40°-100°E and other over 5°N-15°S and 40-100°E. MTTG also defines the monsoon onset date when this changes the sign from negative to positive on the annual cycle and the vice-versa for the monsoon withdrawal.

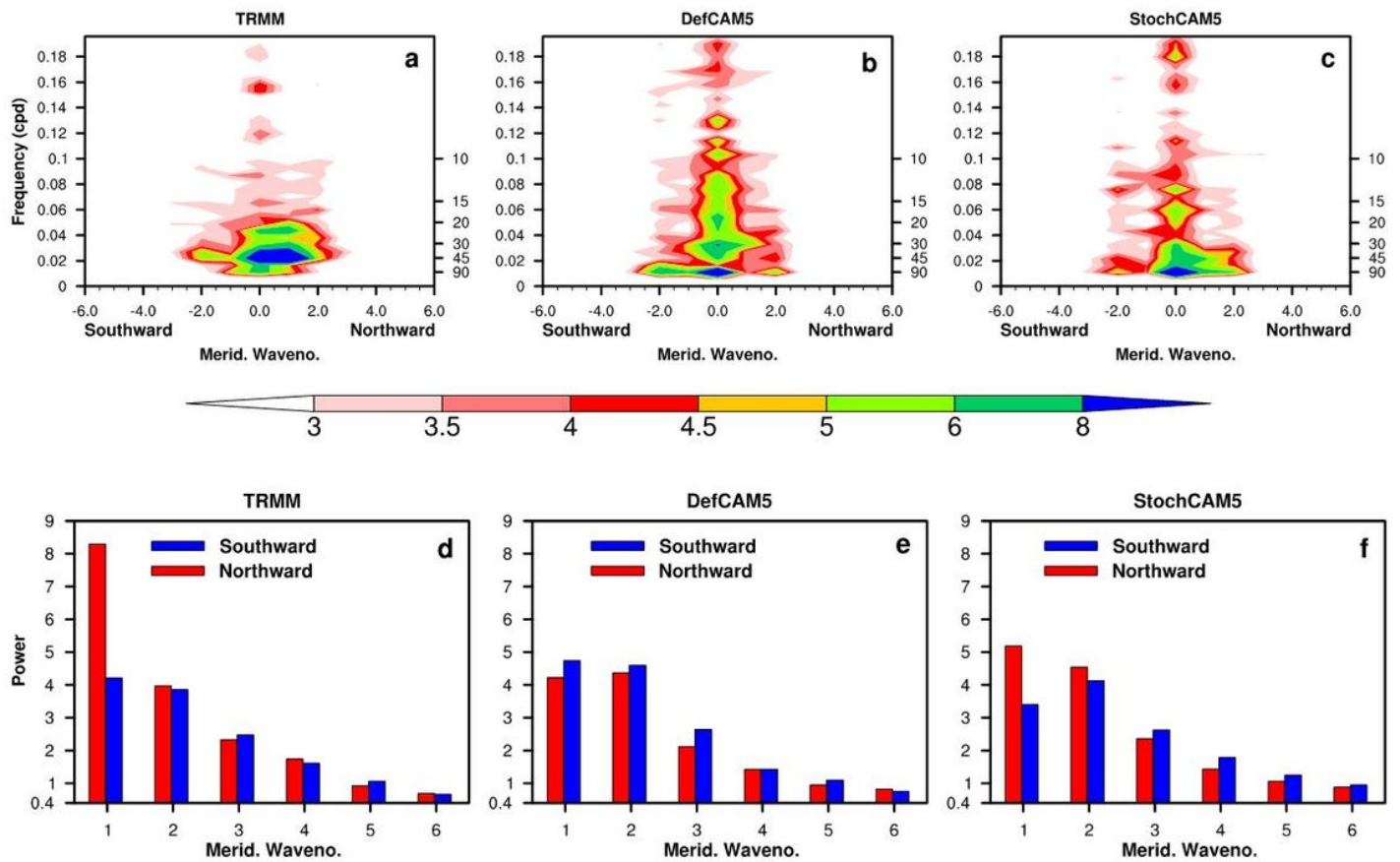


Figure 14

The north-south wavenumber-frequency spectra of precipitation during JJAS for (a) TRMM, (b) DefCAM5, and (c) StochCAM5 over the domain of 15°S-30°N and 60°-95°E. The power of precipitation spectrum separated as the northward and southward component, which is calculated from the north-south wavenumber-frequency spectra of precipitation averaged over 30-90 days period for (d) TRMM, (e) DefCAM5, and (f) StochCAM5.

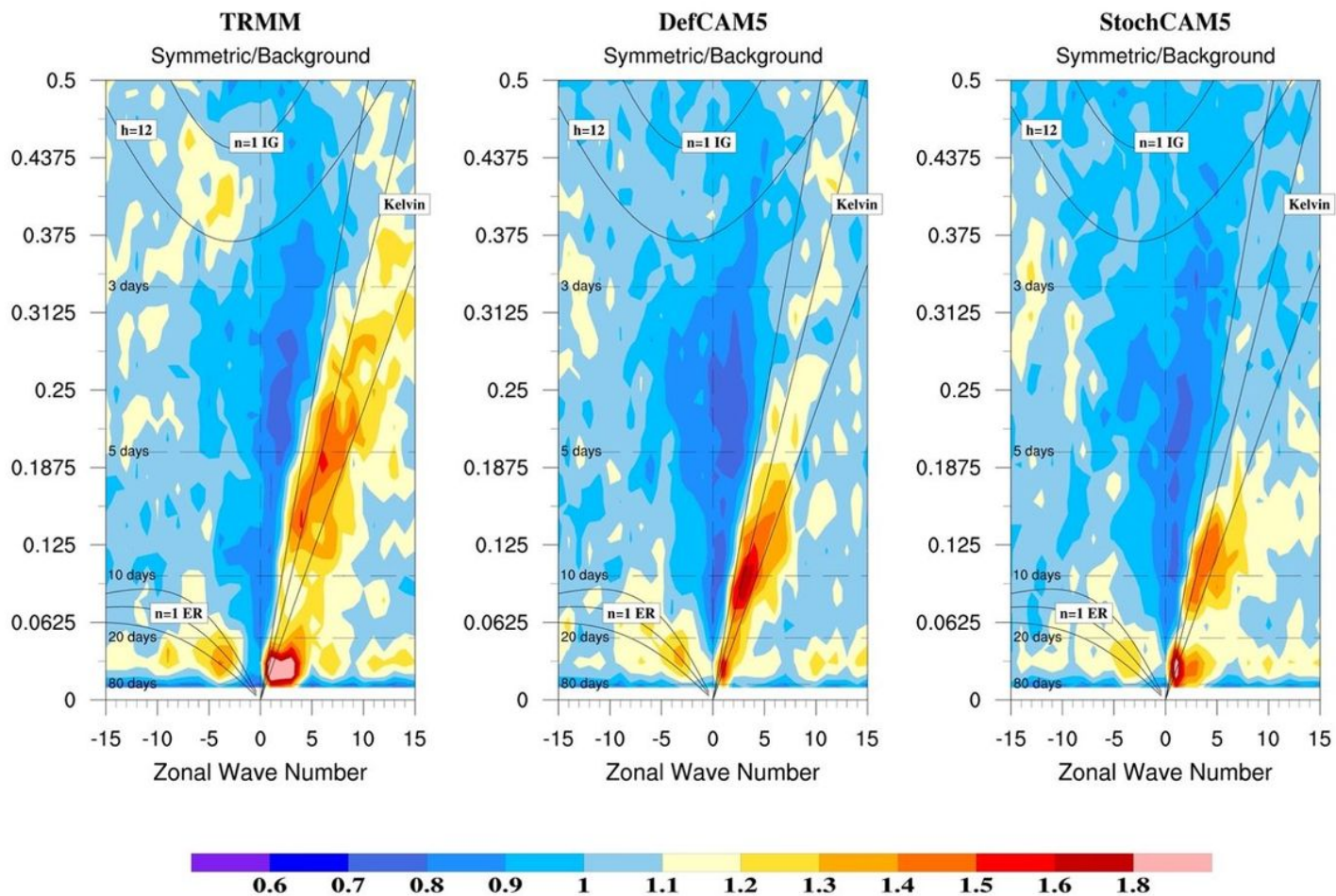


Figure 15

The symmetric component of Wheeler-Kiladis space-time power spectrum for (a) TRMM, (b) DefCAM5, and (c) StochCAM5. It is computed from the daily time-series of total precipitation in the global belt of equatorial region (15°N-15°S) during JJAS.

Supplementary Files

This is a list of supplementary files associated with this preprint. Click to download.

- [CLDYSupplementaryStochEntrainment.docx](#)